

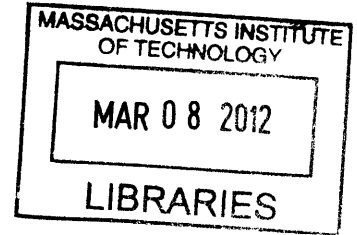
# Interactions among flow, sediment deposition and aquatic vegetation in a channel

By

Lijun Zong

B.A. & M.Eng Civil and Environmental Engineering

University of Cambridge, UK, 2008



**ARCHIVES**

Submitted to the Department of Civil and Environmental Engineering  
in partial fulfillment of the requirements for the degree of  
Master of Science in Civil and Environmental Engineering  
at the

MASSACHUSETTS INSTITUTE OF TECHNOLOGY

September 2011

© 2011 Massachusetts Institute of Technology. All rights reserved.

Signature of Author .....

Department of Civil and Environmental Engineering  
June 27, 2011

Certified by .....

Heidi M. Nepf  
Professor of Civil and Environmental Engineering  
Thesis Supervisor

Accepted by .....

Heidi M. Nepf  
Chairman, Departmental Committee for Graduate Students

# Interactions among flow, sediment deposition and aquatic vegetation in a channel

By

Lijun Zong

Submitted to the Department of Civil and Environmental Engineering

on June 27, 2011 in partial fulfillment of the requirements

for the degree of

Master of Science in Civil and Environmental Engineering

## Abstract

Aquatic vegetation is commonly present in rivers in many forms. This thesis consists of two studies, which examine the flow structure around a patch of emergent, rigid vegetation in a laboratory channel. The vegetation patch is represented by an array of circular cylinders in a staggered arrangement.

The first study investigates flow structure and deposition pattern associated with a long patch of vegetation located at the sidewall of a channel (*i.e.* a partially vegetated channel). Along the flow-parallel edge of the patch, a shear layer is formed due to the velocity difference between the open region and the vegetated region. Coherent vortices are formed via Kelvin-Helmholtz stability in the shear layer, which also induces an edge wave. Both the energetic vortices and the edge wave enhance the lateral mass transport. Particles were introduced to the flow in order to observe the patterns of net deposition within and around the patch. There are two sources of particle flux to the patch: the advection of particles across the upstream leading edge and the lateral dispersion of particles from the adjacent open channel. The relative contribution of these two supplies determines the spatial pattern of net deposition in the patch. A simple model was developed to find the empirical value of the lateral dispersion coefficient. Longitudinal and lateral length scales were found to determine the region where particles cannot be delivered and the net deposition is limited by particle-supply.

In the second study, a circular patch of emergent model vegetation located in the middle of the channel was examined. Its diameter was smaller than the channel width. Velocity measurements and flow visualization were conducted to study the turbulent wake behind the patch. Compared to the wake behind a solid obstruction, the wake behind a patch of vegetation (*i.e.* a porous obstruction) is different. Because of its porosity, some of the flow can pass through the patch, so that directly downstream of the patch there is a region of steady stream-wise velocity with no transverse velocity. This region is called the steady wake and it is also observed from the flow visualization. Unlike the wake behind a solid obstruction, the formation of a von-Karman vortex street behind a porous obstruction is delayed until the end of the steady wake region. As the stem density decreases (*i.e.* the patch becomes sparser), the velocity deficit in the steady wake region decreases and the length of the steady wake increases.

Thesis Supervisor: Heidi M. Nepf

Title: Professor of Civil and Environmental Engineering



## Acknowledgements

First and foremost, I offer my sincerest gratitude to my advisor, Professor Heidi Nepf, for her advice, expertise and patience over the past three years. I have learned and grown so much, and it would not have been possible without her work as my advisor.

Several professors and students were very generous with their support and advice over the past three years. I would like to thank Eric Adams, Ole Madsen, Mitul Luhar, Jeff Rominger and Kevin Zhang for their instruction and time.

I would like to thank MIT machine shop supervisor, Andrew Gallant, for his help and the undergraduate students who worked in the lab, Marina Acevedo, Megan O'Donnell and Tiffany Cheng, for their assistance with the experiments.

I would like to thank my family and all of my friends for their love and support throughout my life.

This material is based upon work supported by a NSF Grant, EAR 0738352. Any opinions, conclusions or recommendations expressed in this material are those of the author(s) and do not necessarily reflect the views of the National Science Foundation.



# Contents

Chapter 1	Introduction	7
1.1	Motivation	7
1.2	Outline	8
Chapter 2	Flow and deposition patterns in a partially vegetated channel	11
2.1	Introduction	11
2.2	General flow structure	14
2.2.1	Flow around a finite patch of vegetation	14
2.2.2	Vegetated-shear-layer and coherent vortices	15
2.3	Transport of suspended particles	17
2.3.1	Delivery of particles into vegetation	17
2.3.2	Equation of transport	18
2.4	Experiment methods	21

2.5	Experimental results of flow measurements	26
2.5.1	Longitudinal profiles	26
2.5.2	Lateral profiles	28
2.6	Experimental results of deposition measurements	32
2.7	Using model to examine the lateral dispersion of particles	36
2.8	Conclusion	38
Chapter 3	Wake structure of a finite patch of vegetation in a channel	39
3.1	Introduction	39
3.2	Experiment methods	42
3.3	Results of the flow field	45
3.3.1	Mean and turbulent velocity profiles	45
3.3.2	Flow visualization	53
3.4	Discussion	58
3.4.1	Steady wake region and growth of the shear layer ( $L_1$ )	58
3.4.2	Magnitude of flow in the steady wake region ( $U_1$ )	63
3.5	Conclusion and areas of future research	64
Chapter 4	Conclusion	67
References		69

# Chapter 1

## Introduction

### 1.1 Motivation

Aquatic vegetation exists in many river systems in many forms: river floodplains, vegetated islands in rivers, floating vegetation mats. It is a very important element in the ecosystem, because vegetation not only provides habitat to many animals including fishes and birds, produces oxygen for aquatic organisms, but also improve water quality and clarity by taking up nutrients, and by trapping heavy metals and suspended particles (Gacia and Duarte 2001; Schultz et al. 2003; Brookshire and Dwire 2003; Windham et al. 2003; Moore 2004; Cotton et al. 2006; Widdows et al. 2008). Finally, coastal vegetation can protect shorelines from erosion and storm surge by dampening waves and currents (*e.g.* Massel et al. 1999; Turker et al. 2006; Gedan et al. 2011)

Historically, aquatic vegetation had been removed in order to increase the flood flow conveyance in the channel. However, the removal of vegetation caused many problems, including increased bank failure, degraded water quality and unbalanced ecosystem. Over the past twenty years, river restoration has become one of the most important advances in river management. The common efforts of river restoration focus on stream bank stabilization, enhancing riparian buffers by planting vegetation, restoring meanders,

removing man-made structures (dams) and stocking the river with fish or other living organisms (Muhar et al. 1995; De Waal et al. 1998; Hill et al. 1998; Stromberg 2001). In river restoration, vegetation is one of the most effective tools. For example, one method of restoring meanders is to introducing vegetation in alternating locations to divert the flow and cause sediment deposition (Bennett et al. 2002).

The most immediate effect of vegetation is that it changes the mean velocity distribution and turbulence structure by producing additional hydrodynamic drag. The flow structure affects the distribution of sediments, which in turn influences the spatial structure of the vegetation. Therefore it is important to have a good understanding of the interaction among vegetation, flow and sediment distribution.

## 1.2 Outline

Many laboratory experiments and numerical analyses have been conducted to study how vegetation impacts flow and sediment transport. Depending on the environment in which the vegetation grows and the species, aquatic vegetation can be classified into submerged, emergent and floating vegetation. There are also variations in stem stiffness and morphology. In this thesis, I am primarily interested in the flow and the deposition patterns associated with rigid, emergent vegetation. Two studies are discussed in this thesis. Experiments were conducted in a laboratory flume. The emergent vegetation patch was constructed from a staggered array of rigid circular cylinders, because circular cylinders provide a reasonable morphological approximation of the stem region of emergent vegetation like reeds and rushes. The distribution of cylinders is homogenous within the patch. The cylinder array is described by the following parameters: the cylinder diameter,  $d$ , the number of cylinders per unit bed area,  $n$ , and the frontal area per unit volume,  $a = nd$ , and the average solid volume fraction of the array,  $\Phi = n(\pi d^2/4) \approx ad$ .

In Chapter 2, the flow field and the spatial pattern of deposition in a partially vegetated channel (mimicking a river-vegetated-bank system) are discussed. Laboratory experiments were conducted to measure the mean flow velocity and turbulence structure within and around the vegetated region. Along the flow-parallel edge of the vegetated region, coherent vortices are formed due to the velocity difference between the open region and the vegetated region. These energetic coherent vortices dominate momentum and mass exchange between the vegetation and the adjacent open flow. They also induce an edge wave, which enhances the lateral mass transport into the vegetated region from the adjacent open channel. Particles were introduced to the flow in order to observe the spatial patterns of deposition. Net deposition can be limited by resuspension and by the particle supply. Resuspension is positively related with the turbulence intensity. Particle supply depends on the spatial structure of the vegetation patch and the flow

condition. In this case, there are two sources of particle flux to the patch: the advection of particles across the upstream leading edge and the lateral dispersion of particles from the adjacent open channel. The relative contribution of these two supplies determines the spatial pattern of net deposition in some part of the vegetated region, where no resuspension occurs. The longitudinal and lateral length scales corresponding to the two particle supplies are discussed. Therefore an area within the vegetation, where no particles can be delivered, was determined. In that area, the particle concentration is lower than that in the other part of the vegetation, which results in a lower deposition.

In Chapter 3, a circular patch of emergent model vegetation located in the middle of the channel is examined. The patch diameter is smaller than the channel width. Velocity measurements and flow visualization were conducted in the same flume used in Chapter 2 to study the two-dimensional turbulent wake behind the vegetation patch. Compared to the wake behind a solid obstruction, the wake behind the patch (*i.e.* a porous obstruction) is longer, because it has a region of steady stream-wise velocity directly behind the patch. This region is called the steady wake. The formation of a von-Karman vortex street behind the patch is delayed until the end of the steady wake region. This chapter discusses the cause of the steady wake region, the velocity inside the steady wake region and its length. Comparisons to the solid body case and previous research are also discussed. This study of the wake structure behind a short vegetation patch will help to understand the deposition/erosion patterns and therefore the potential evolution of the spatial structure of the bed and the vegetation patch.



# Chapter 2

## Flow and deposition patterns in a partially vegetated channel

### 2.1 Introduction

By baffling the flow and reducing bed stress, a finite patch of vegetation creates a region of sediment retention (*e.g.* Abt et al. 1994; Lopez and Garcia 1998; Palmer et al. 2004; Cotton et al. 2006). In some channels vegetation patches have been shown to retain up to 80% of the sediment in transit downstream (Sand-Jensen 1998). The tendency for reduced mean flow and reduced turbulence within the patch, relative to the free stream, suggests that particles that remain in suspension in the free stream may deposit after entering the vegetation patch. Fonseca et al. (1983) observed that finite patches of seagrass are associated with local bed maxima. Heavy metals and other contaminants are preferentially associated with fine grain sediments which are usually in suspension, and the transport of suspended particles to a patch of vegetation depends on the flow structure around the patch. Inside the vegetation patch, the rate of net deposition of suspended particles depends on the particles characteristics, the flow condition, and the delivery of particles to the patch (*i.e.* particle-supply). Deposition within the vegetation can be limited by resuspension or by particle supply. Strong turbulence can generate a lot of resuspension and therefore

reduce the net deposition rate. Limited particle supply will lead to a low particle concentration inside the vegetation and therefore a low deposition rate.

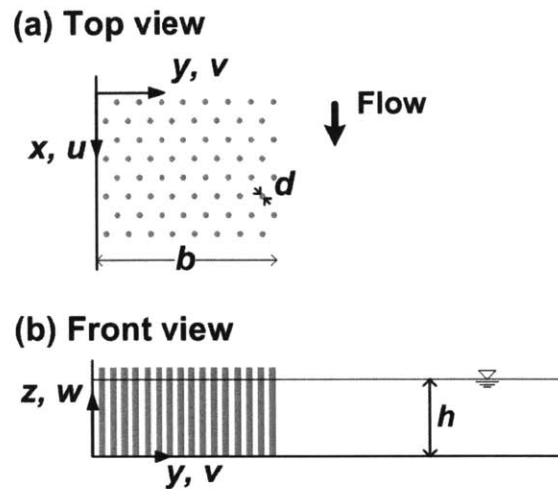


Figure 2.1 A schematic of the partially vegetated channel, (a) top view, (b) front view. The longitudinal, transverse, and vertical coordinates and velocity are  $(x, u)$ ,  $(y, v)$  and  $(z, w)$ , respectively. Emergent model stems of diameter  $d$  fill a region of lateral width  $b$ . The flow depth is  $h$ .

The problem of interest in this chapter is that of flow structure and spatial pattern of deposition in the partially vegetated channel, a setup mimicking the river vegetated-bank system (Fig. 2.1). Due to the additional hydrodynamic drag produced by the vegetation, mean flow rate inside vegetation is lower than in the open water, which in turn creates a shear-layer at the flow-parallel interface between the vegetated region and the open water. Like in a free shear layer, coherent vortices form via the Kelvin-Helmholtz instability in this vegetated-shear-layer (White and Nepf 2007 & 2008). These energetic vortices dominate mass and momentum exchange between the vegetation and the adjacent open flow. These coherent turbulent structures are also important for the hydrologic and ecological processes in the system, *e.g.* nutrient supply, pollutant transportation (Macklin 1996).

Suspended particles carried by the stream enter the patch from the leading edge. As particles traveling through the patch, they are lost to deposition and particle concentration decreases. It is reasonable to assume that the concentration in the open water will not decline as much as in the vegetation because the fast flow can generate resuspension. Therefore a concentration gradient at the flow-parallel interface between the vegetation and open water is created, which leads to a lateral flux of particles into the vegetation patch through diffusion. This lateral transport of particles is enhanced by the coherent turbulent structures formed at the flow-parallel interface. Experiments had been carried out in a laboratory flume partially filled with model emergent vegetation (piercing water surface).

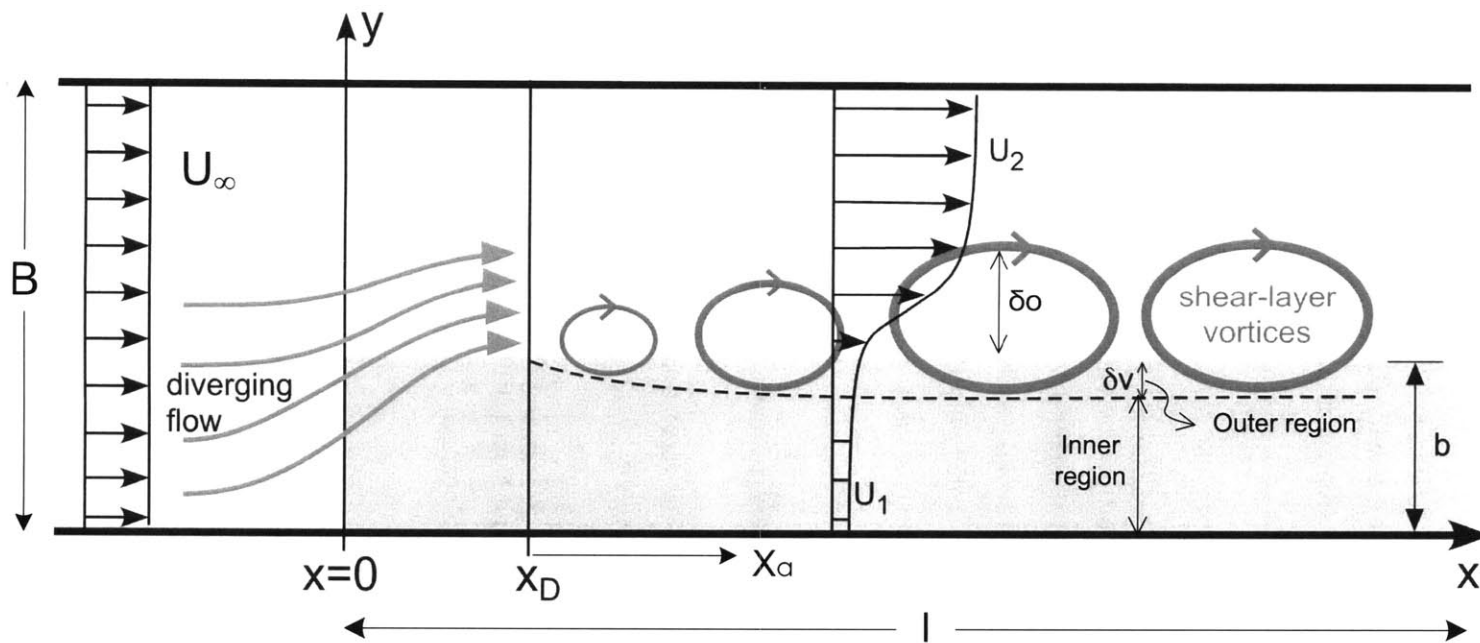


Figure 2.2 Conceptual picture of the flow field near a finite patch of vegetation. Flow divergence begins upstream of the patch and extends some distance into the patch. The position  $x_D$  indicates the end of the diverging flow and the beginning of the shear-layer development at the flow-parallel edge of the patch. The shear-layer penetrates a distance,  $\delta_v$ , into the patch. The velocity within the patch,  $U_1$ , is laterally uniform. The advection distance,  $x_a = U_1 T_s$ , is measured from the end of the diverging flow region.

## 2.2 General flow structure

### 2.2.1 Flow around a finite patch of vegetation

A schematic graph of the flow field is shown in Figure 2.2.  $x$  denotes the stream-wise direction, with  $x=0$  at the leading edge of the vegetated region. The lateral coordinate is  $y$ , with  $y=0$  at the sidewall of the channel. The flume extends from  $0 < y < B$ , with  $B$  is the width of the channel. The vegetated region is from  $0 < y < b$  and  $0 < x < l$ , where  $b$  and  $l$  represent the width and length of the patch, respectively, and  $l > b$ .

Because the vegetation is a region of high drag, much of the flow approaching the patch from upstream is diverted away from the patch. The diversion begins upstream of and extends some distance into the vegetation patch. The end of the flow diverging region is denoted by  $x_D$ . Rominger and Nepf (2011) describe the velocity deceleration through a long (length much larger than patch width) patch located in the middle of a channel. From scaling analysis and experimental results, they found that the length of upstream adjustment region is scaled with the patch half-width,  $b$ , and the length of interior adjustment region,  $x_D$ , depends on the dimensionless parameter,  $C_D ab$ , called the patch flow-blockage. The scaling of  $x_D$  on  $C_D ab$  is

$$x_D = \frac{(5.5 \pm 0.4)}{C_D a} \left[ 4 + (C_D ab)^2 \right]^{1/2} \quad (2.1)$$

where  $C_D$  is the bulk drag coefficient for the vegetation. For low flow-blockage ( $C_D ab < 2$ ),  $x_D$  is scaled with  $(C_D a)^{-1}$ . For high flow-blockage ( $C_D ab > 2$ ),  $x_D$  is scaled with  $b$  only.

Beyond  $x_D$ , a final interior velocity ( $U_1$ ) is reached within the patch and the steady velocity in the open region is  $U_2$  (Fig. 2.2). Rominger and Nepf (2011) show that the magnitude of  $U_1$  also depends on the flow-blockage ( $C_D ab$ ). For high flow-blockage ( $C_D ab > 2$ ),  $U_1$  is a function of the patch solid volume fraction ( $\Phi$ ),

$$\frac{U_1}{U_\infty} = \sqrt{\frac{C_f (1-\Phi)}{h C_D a}} = \sqrt{\frac{C_f d}{C_D h} \left( \frac{1}{\Phi} - \Phi \right)} \quad (2.2)$$

For low flow-blockage ( $C_D ab < 2$ ),  $U_1$  depends on the solid volume fraction ( $\Phi$ ) and the width of the patch ( $b$ ),

$$\frac{U_1}{U_\infty} = \frac{1}{U_\infty} \sqrt{\frac{U_*^2 2(1-\Phi)}{b C_D a}} \quad (2.3)$$

where  $u_*$  is the friction velocity at the flow-parallel edge of the patch, i.e.  $u_*^2 = -\overline{U'V'}$  at  $y = b$ . The velocity difference between the vegetated region and the open region ( $U_1$  and  $U_2$ ) creates a shear-layer and therefore generates the coherent vortices at the flow-parallel interface ( $y = b$ ).

## 2.2.2 Vegetated-shear-layer and coherent vortices

The characteristics of coherent vortices in a vegetated-shear-layer are described in White and Nepf (2007, 2008). In a free shear-layer, the shear-layer vortices grow continually downstream predominantly through vortex pairing (*e.g.* Winant and Browand 1974). However, in a vegetated shear-layer, the vortices reach a fixed scale and a fixed penetration into the vegetated region at a short distance from the leading edge of the patch (Ghisalberti and Nepf 2004). Based on scaling and laboratory experiments done by White and Nepf (2007), the vortex penetration scale is inversely proportional to the drag, as parameterized by  $C_D a$ ,

$$\delta_v = \max [ 0.5 (C_D a)^{-1}, 1.8d ]. \quad (2.4)$$

It is important to note that the penetration scale is not a function of the flow speed, except through a weak dependence of  $C_D$  on the local velocity.

The shear layer extends into the open channel over the length-scale  $\delta_o$ . White and Nepf (2007) show that  $\delta_o \sim h/C_f$ , where  $h$  is the flow depth and  $C_f$  is the bed friction. There is no direct relation between  $\delta_v$  and  $\delta_o$ .

The penetration scale ( $\delta_v$ ) segregates the vegetation patch into two regions. Within the penetration distance (the outer region,  $b - \delta_v < y < b$ , in Fig. 2.2), turbulent transport and water renewal are enhanced by the shear layer vortices. In contrast, within the inner region ( $0 < y < b - \delta_v$ ), turbulence is generated only within the wakes of individual stems, and thus has significantly smaller scale, set by the stem diameter and spacing. As a result, turbulent diffusion in the inner region is ten to a hundred times slower than in the outer region (Ghisalberti and Nepf 2005; Nepf et al. 2007).

The turbulent diffusion of the inner region can be estimated from a model developed for flow within homogeneous, emergent vegetation (Nepf 1999; Lightbody and Nepf 2006; Tanino and Nepf 2008). For solid volume fractions up to 10%, Nepf et al. (2007) suggests the turbulent diffusivity is scaled with the velocity inside the patch,  $U_1$ , and with the size of the individual stems,  $d$ .

$$D_{t,i} = 0.17 U_1 d. \quad (2.5)$$

The turbulent diffusivity in the outer region,  $D_{t,o}$ , scales on the velocity difference  $\Delta U = U_2 - U_1$ , and on the shear layer width,  $t_s$ .

$$D_{t,o} = \beta \Delta U t_s, \tag{2.6}$$

with  $\beta = 0.02$  ( $\pm 15\%$ ) for rigid vegetation and solid volume fractions between 1% and 4% (Ghisalberti and Nepf 2005). Because  $D_{t,o}$  is generally at least one order of magnitude larger than  $D_{t,i}$ , it is reasonable to assume that the lateral turbulent flux of particles into the patch is limited by the inner layer transport.

The vortices not only enhance the turbulence in the outer region relative to the inner region, they also generate a wave motion across both the outer and the inner regions, as shown schematically in Figure 2.3. The center of each vortex is a point of low pressure, which draws fluid from within the patch toward the edge as it passes. The progression of the vortices (and associated low pressure points) passing along the vegetation edge generates a wave response within the patch that is predominantly manifest in an oscillating lateral motion with a frequency fixed by the frequency of vortex passage. It is likely that these strong lateral motions enhance the lateral mass transport into patch (*e.g.* sediment, nutrient).

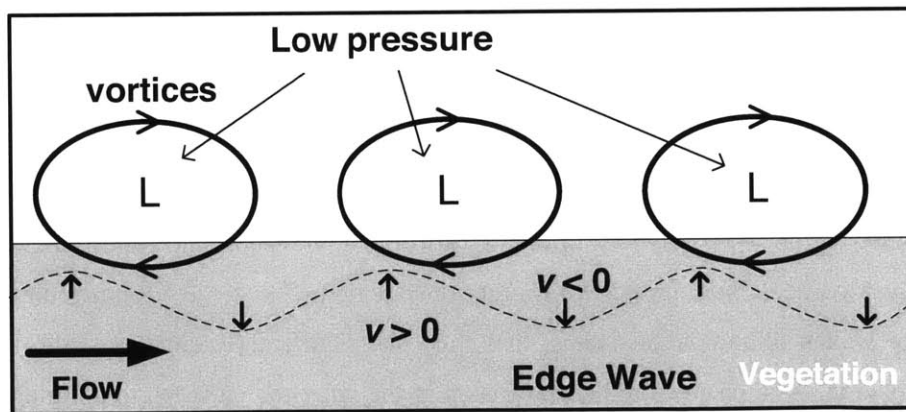


Figure 2.3 Schematic of edge-wave generation. Each vortex core is a pressure minimum (L). The migration of the low pressure point along the flow-parallel edge generates a wave response in the patch, which is depicted by the dashed streamline. The maximum outward velocity ( $v > 0$ ) lags the minimum pressure by 90 degrees, as expected by wave theory.

## 2.3 Transport of suspended particles

### 2.3.1 Delivery of particles into vegetation

Based on the flow structure discussed in the previous section, in addition to advection through the leading edge of the patch, the shear-layer vortices at the flow-parallel edge can deliver particles into the patch through lateral turbulent diffusion and the edge-wave dispersion. For the particles entering through the leading edge of the patch, the distance (denoted as  $x_a$  in Fig. 2.2) over which they travel before depositing is determined by the velocity inside the patch,  $U_1$ , and the settling time scale,  $T_s = h/w_s$ , where  $h$  is the water depth and  $w_s$  is the particle settling velocity.

$$x_a = U_1 T_s = \frac{U_1 h}{w_s} \quad (2.7)$$

Since we assume that, in the flow diverging region ( $x < x_D$ ), net deposition is limited by resuspension, the particle concentration in this region is close to the concentration in the open region.  $x_a$  is measured from the position of  $x_D$  (Fig. 2.2). Therefore at position  $x \gg x_D + x_a$ , the particle concentration is much smaller than that at  $x \leq x_D$ .

As the particle concentration inside the patch decreases with the distance from  $x_D$ , and the concentration in the adjacent open region remains constant due to resuspension, a lateral concentration gradient is achieved, which leads to a lateral flux of particles towards the patch. The mass transfer in the outer region ( $b - \delta_v < y < b$ ) is so rapid that it is reasonable to assume the particle concentration in the outer region is same as in the adjacent open water. Particles can be delivered to the inner region through turbulent diffusion and the lateral wave motion. Molecular diffusion plays a negligible role for the particle sizes and flow conditions considered here, therefore it is not included. It is not yet clear how to parameterize the edge-wave dispersion. Therefore only the turbulent diffusion is discussed in this section.

For the lateral transport by turbulent diffusion in the inner region, a diffusion length scale,  $\delta_{max}$ , can be defined as the maximum distance particles can travel into the inner region. If the open channel provides a constant concentration boundary condition,  $C_o$ , lateral diffusion yields an *erfc* profile within the inner region (*e.g.* Fischer et al. 1979, Section 2.3.2). For this distribution the concentration boundary layer defined as the point where the concentration drops to  $C = 0.005 C_o$ , is described by  $\delta = 4\sqrt{D_{t,i}t}$ , in which  $D_{t,i}$  is the lateral turbulent diffusion coefficient in the inner region. The maximum distance is constrained by the settling time scale,  $T_s$ , such that

$$\delta_{max} = 4\sqrt{D_{t,i}T_s} = 4\sqrt{\frac{0.17U_1 dh}{w_s}} \quad (2.8)$$

If the patch length,  $l$ , is long enough ( $l \gg x_D + x_a$ ) and the width,  $b$  is wide enough ( $b > \delta_v + \delta_{max}$ ), there will be a region within the patch that cannot be reached by particles supplied from the upstream or from the flow-parallel edge. If such a region exists within the patch, then the deposition will be supply limited. In addition to supply-limited deposition, deposition can also be limited by resuspension in which case the turbulence is strong enough to resuspended particles and reduces the net deposition rate. Both cases are observed in this study.

### 2.3.2 Equation of transport

In this section a simple numerical model is used to illustrate how the advection length scale,  $x_a$ , and the diffusion length-scale,  $\delta_{max}$ , influence the deposition pattern within a patch. The flow field used in the model is based on observations made in a previous study, upon which Figure 2.2 is based (Zong and Nepf 2010). As in Figure 2.2, the coordinate system is  $x = 0$  at the leading edge and  $y = 0$  at the channel wall, and the patch extends from  $y = 0$  to  $y = b$ . The flow field is two-dimensional with the mean longitudinal and transverse velocities denoted by  $\bar{u}$  and  $\bar{v}$ , respectively. For simplicity, we only consider the patch domain downstream of the diverging region ( $x > x_D$ ), where the flow is laterally uniform within the patch, *i.e.*  $\bar{u} = U_1 \neq f(x, y)$  and  $\bar{v} = 0$ . The loss of suspended sediment associated with deposition is modeled as a first-order process with rate constant  $k = w_s/h$  (*e.g.* as in Hosokawa and Horie 1992). For  $x > x_D$ , we assume there is no resuspension, because Zong and Nepf (2010) note that the bed stress in the patch interior is far below the critical value for resuspension. Finally, we assume that the longitudinal dispersion is negligible compared with advection. The steady, depth-averaged equation for suspended sediment concentration within the patch is then,

$$U_1 \frac{\partial C}{\partial x} = \frac{\partial}{\partial y} \left( D_y \frac{\partial C}{\partial y} \right) - kC \quad (2.9)$$

Since the transport across the outer patch region ( $b - \delta_v < y < b$ , Fig. 2.2) is much faster than that in the inner patch region ( $0 < y < b - \delta_v$ , Fig. 2.2) as discussed above, we assume that the particle concentration in the outer region is the same as the free stream,  $C_o$ , so that the boundary of our solution domain will be at the edge of the inner region ( $y = b - \delta_v$ ). The boundary conditions are then,

- (i) concentration at  $x = x_D$  is equal to the open channel,  $C(x = x_D) = C_o$ ;
- (ii) concentration in the outer region is equal to the open channel,  $C(y \geq b - \delta_v) = C_o$ ;
- (iii) no flux through the sidewall,  $\partial C / \partial y = 0$  at  $y = 0$ .

The lateral flux across the inner patch region ( $y < b - \delta_v$ ) is associated with turbulent diffusion,  $D_y = D_{t,i}$ . Note that the effect of edge-wave motion is not included here. The following parameter values based

on Zong and Nepf (2010) are adopted,  $d = 0.6$  cm,  $U_T = 0.5$  cm/s,  $h = 10$  cm,  $b = 40$  cm,  $\delta_v = 5$  cm and  $w_s = 0.01$  cm/s. From Eq. (2.5),  $D_y = D_{t,i} = 0.05$  cm<sup>2</sup>/s.

The simulated suspended particle concentration inside the patch (*i.e.* the numerical solution of Eq. 2.9) is shown in Figure 2.4a. Particles enter the modeled region at a suspended sediment concentration  $C_o$ . As particles travel downstream, some are deposited, so that the water column concentration diminishes with distance from the leading edge. The decline is most apparent close to the wall ( $y = 0$ ), because lateral particle flux maintains a high concentration near the flow-parallel edge ( $y = b$ ). After the supply from upstream is depleted by deposition, the lateral flux becomes the only supply of new particles to the patch. Considering different longitudinal positions, as shown in Figure 2.4b, reveals the interplay of particle sources from advection and lateral diffusion. The vertical dashed lines in Figure 2.4b mark the length-scales  $\delta_v$  and  $\delta_{max}$ . The region to the left of both dashed lines, *i.e.*  $y < (b - \delta_v - \delta_{max})$ , is supplied with suspended sediment only by advection from the leading edge. The rest of the patch,  $y > (b - \delta_v - \delta_{max})$ , is supplied with suspended particles by both advection and lateral diffusion. At distances much less than the advection length-scale, *e.g.*  $(x - x_D)/\chi_a = 0.1$  in Figure 2.4b, the suspended particle concentration within the patch is similar in magnitude to that at the leading edge ( $C_o$ ), because little deposition has occurred by this point; and the concentration is laterally uniform over most of the patch width, reflecting the laterally uniform flow field. Far downstream of the advection length-scale, *e.g.*  $(x - x_D)/\chi_a = 5$ , nearly all particles that entered across the leading edge have settled out, and the region of the patch supplied only by advection from the leading edge,  $y < (b - \delta_v - \delta_{max})$ , has a very low concentration, specifically  $C < 0.005 C_o$ . This corresponds to the region  $y/b < 0.2$  in Figure 2.4b. Particles continue to be supplied by lateral diffusion in the region  $y/b > 0.2$ , and in this region the concentration profile follows the *erfc* shape expected for diffusion from a constant source, with concentration highest at the patch edge and decreasing toward the wall over the distance  $\delta_{max}$  (Fischer et al. 1979, Section 2.3.2). If resuspension within the patch is negligible, the spatial pattern of deposition within the patch will mirror the spatial distribution of suspended sediment concentration. In the experiments that follow, observed deposition patterns have a dependency on the parameter  $(x - x_D)/\chi_a$  that is consistent with the model described here.

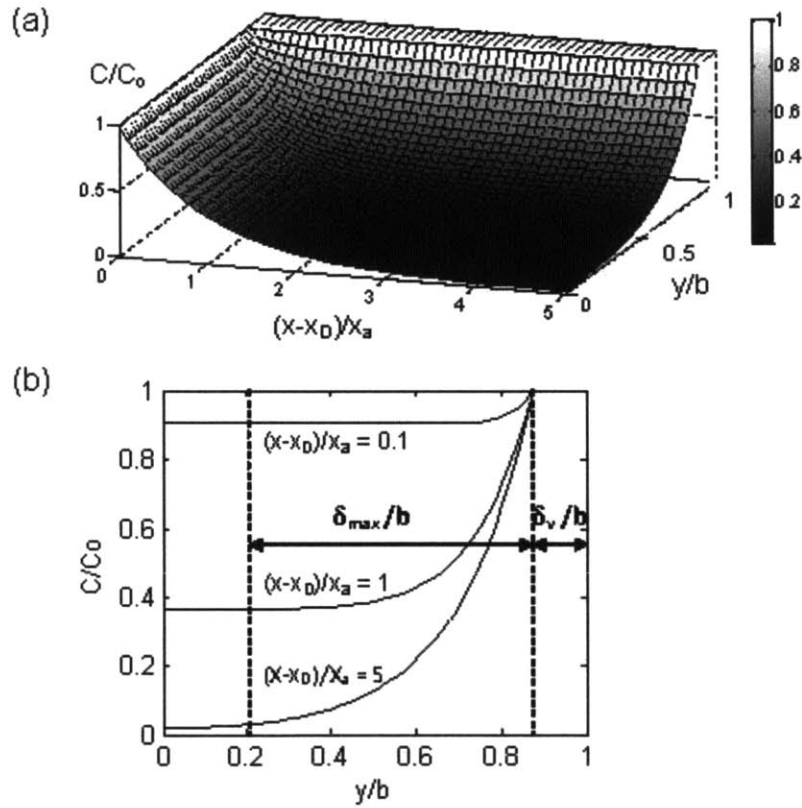


Figure 2.4 (a) Simulated suspended particle concentration,  $C(x,y)$ , normalized by the upstream concentration,  $C_0$ , in the vegetation patch at  $x > x_0$ ; (b) Simulated lateral concentration profiles across the patch width ( $0 < y < b$ ).

## 2.4 Experiment methods

Experiments were conducted in a 16-m long re-circulating flume with a test section that is 1.2 m wide and 13 m long (Fig. 2.5a and b). The bed of the flume is horizontal. The flume was partially filled with a patch of model emergent vegetation, constructed with a staggered array of circular cylinders of diameter  $d = 6$  mm. The patch was 0.4m wide (1/3 of the flume width), 10m long, and began 2 m from the start of the test section. The cylinders were held in place by perforated PVC baseboards that extended over the entire flume width. Two stem densities were considered, with  $a = 0.04 \text{ cm}^{-1}$  and  $0.20 \text{ cm}^{-1}$ , corresponding to solid volume fractions of  $\Phi = 0.02$  and  $0.10$ , respectively. These values are representative of densities observed in aquatic vegetation. For example, in mangroves  $\Phi$  can be as high as 0.45 (Mazda et al. 1997), submerged grasses are relatively sparse, with  $\Phi = 0.01$  to  $0.1$  (Gambi et al. 1990; Chandler et al. 1996; Ciruolo et al. 2006), emergent grasses have been observed with  $\Phi = 0.001 - 0.02$  (Valiela et al. 1978; Leonard & Luther 1995).

Three flow rates were tested for each patch density, with upstream channel velocities of  $U_\infty = 5.0$  cm/s, 9.0 cm/s and 11.6 cm/s. A weir at the downstream end of the test section controlled the water depth. To characterize the flow field, velocity measurements were taken using two Nortek Vectrino ADVs, each with a sampling volume 6 mm across and 3 mm high. The probes were mounted on a platform that could be moved along and across the flume. Since the probes were manually positioned, the positioning accuracy was  $\pm 0.5$  cm in the  $y$  direction and  $\pm 1$  cm in the  $x$  direction. A longitudinal transect was made through the centerline of the vegetation patch ( $y = 20$  cm), shown in Figure 2.5b, starting 2 m upstream of the patch ( $x = -2$  m) and extending to the end of the patch ( $x = 10$  m). In addition, lateral transects were made downstream of the diverging region ( $x > x_D$ ). At each measurement point the probe was positioned mid-way between adjacent cylinders within the array pattern. At each position the instantaneous longitudinal ( $u(t)$ ) and lateral ( $v(t)$ ) components of velocity were recorded at mid-depth for 240s at a sampling rate of 25Hz. Each record was decomposed into its time-average,  $(\bar{u}, \bar{v})$ , and fluctuating components ( $u'(t), v'(t)$ ). The over bar denotes the time-average. The intensity of turbulent fluctuations was estimated as the root-mean-square of the fluctuating velocity,  $u_{rms} = \sqrt{\overline{(u')^2}}$  and  $v_{rms} = \sqrt{\overline{(v')^2}}$ . The mean velocity had an uncertainty of  $\pm 0.1$ cm/s. Measurements made in still water determined that the instrument noise,  $u_{rms,noise} = 0.3$ cm/s, which set the lower limit at which turbulent intensity can be resolved.

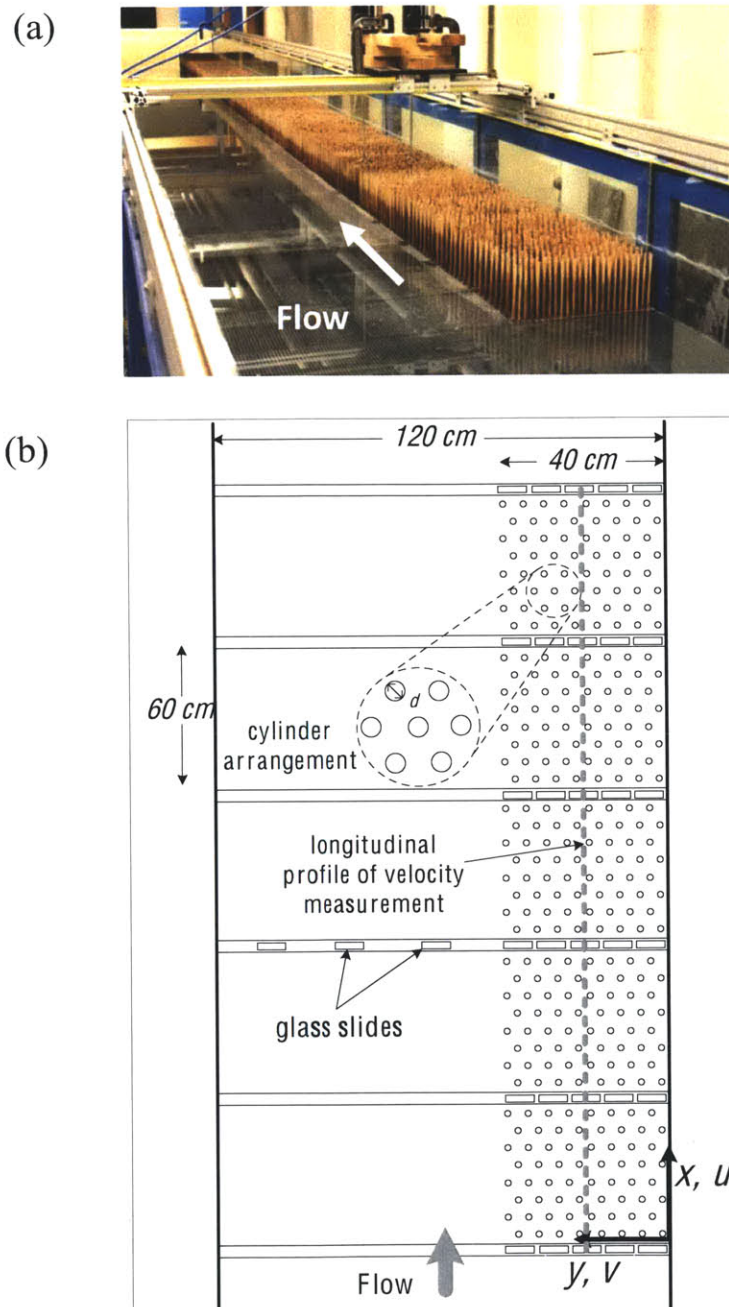


Figure 2.5 (a) Picture of the flume partially filled with an array of dowels. Flow is from bottom to top of page; (b) Top view of channel over the first 3m of the vegetated zone, the full patch length is 10 m, the distribution of microscope slides is repeated along the patch length. Note that lateral deposition profiles were not taken at every longitudinal position for every condition.

The model sediment was scaled to provide a desired ratio of settling velocity,  $w_s$ , to bed friction velocity,  $u_*$ , such that deposition would be favored in the vegetation ( $w_s/u_* > 0.1$ ), but not in the open channel ( $w_s/u_* < 0.1$ , as in Julien, 1995). From preliminary measurements, the average velocity in the open channel and in the vegetation was roughly 20 cm/s and 0.5 cm/s, respectively. Using the bed friction coefficient ( $C_f = 0.006$ ) measured in previous studies over the same baseboards (White and Nepf, 2007 & 2008),  $u_*$  is anticipated to be 1.5 cm/s and 0.04 cm/s, in the open channel and vegetation, respectively. Based on these estimates and the criteria above, I sought a particle with a settling velocity on the order of 0.01 cm/s. I selected a glass bead with diameter  $d_p$  of 12 $\mu$ m and density  $\rho_p$  of 2.5g/cm<sup>3</sup> from Potters Industry, Inc., Valley Forge, Pa. The particles are spherical, so that the settling velocity,  $w_s = 0.01$  cm/s, can be calculated using the formula from Soulsby (1997),

$$w_s = \frac{\nu}{d_p} \left[ \left( 10.36^2 + 1.049 \left( \frac{g(s-1)}{\nu^2} \right) d_p^3 \right)^{1/2} - 10.36 \right] \quad (2.10)$$

with  $\nu$  is the kinematic viscosity of water,  $\nu = 0.01$  cm<sup>2</sup>/s for temperature of 20°C, and  $s$  is the specific gravity of the particle,  $s = \rho_p/\rho_{\text{water}} = 2.5$ , and  $g$  is the gravitational acceleration,  $g = 980$  cm<sup>2</sup>/s.

To begin the deposition study, 550g of the model sediment were vigorously mixed with water in small containers. The mixture was poured across the width of the upstream feeder tank and stirred. From visual inspection, the particles mixed over the width and depth of the flume within a minute, which was much shorter than the 8-hour duration of the experiment. The particles circulated with the water through the closed flow system. During each experiment, the concentration in the water was measured every two hours by filtering a 500 ml water sample taken upstream of the patch. Figure 2.6 shows the suspended sediment concentration as a function of time for several cases.

The net deposition was measured using rectangular microscope slides (7.5 cm  $\times$  2.5 cm), which were placed on the bed of the flume (Fig. 2.5b). The slides are smooth and have a surface roughness close to that of the PVC boards. The dry slides were weighed before placement. At the end of the experiment, the pump was first shut off and then the flume was slowly drained over a 20-minute time span. The drainage was done slowly to prevent scouring from the slides. I let the slides sit in the flume for three or four days, until the surfaces of the slides were dry and the slides could be moved without disturbing the deposited particles. The slides were carefully picked up by hand, placed on trays, and baked overnight in an oven. Finally, the slides were reweighed. The weight of a slide after the experiment minus the weight before was taken as the net mass deposition. From visual inspection, the deposition on the slides was uniform, with no obvious edge effects. The deposition per area measured by slides of different size is also compared. The deposition per area was the same within uncertainty, indicating that the slide size did not

influence the measurement. Three replicate experiments were done for each flow condition and patch density. The uncertainty in net deposition was estimated from the standard error among replicates at each position in the flume. The maximum deposition observed inside the patch for each case is recorded in Table 2.1.

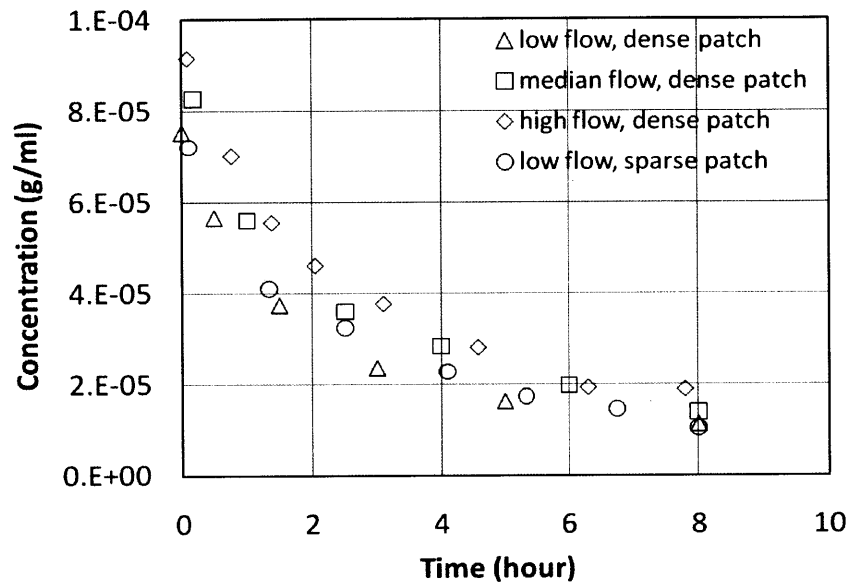


Figure 2.6 Concentration,  $C_o$ , measured at the upstream end of the test section.

Table 2.1 Summary of experimental parameters

	Dense Patch ( $\Phi = 0.10$ )			Sparse Patch ( $\Phi = 0.02$ )		
	low flow	medium flow	high flow	low flow	medium flow	high flow
$\alpha$ ( $m^{-1}$ )	20	20	20	4	4	4
$h$ (cm) $\pm 0.5$ cm	12.0	13.0	14.0	12.0	13.0	14.0
$U_x$ (cm/s) $\pm 0.5$ cm/s	5.0	9.0	11.6	5.0	9.0	10.7
$U_1$ (cm/s) $\pm 0.1$ cm/s	0.1	0.2	0.3	0.6	1.1	1.4
$U_2$ (cm/s) $\pm 0.5$ cm/s	9.0	16.2	20.9	8.5	15.0	19.0
$Re_d = U_1 d/\nu$	6	12	18	36	66	84
$Re_h = U_1 h/\nu$	120	260	420	720	1430	1960
$x_D$ (cm) $\pm 10$ cm	200	200	200	300	300	300
$\delta_x$ (cm) from Eq.(2.4)	2.5	2.5	2.5	12.5	12.5	12.5
$x_d$ (cm) from Eq.(2.7)	120	260	420	720	1430	1960
$D_{t,i}$ ( $cm^2/s$ ) from Eq.(2.5)	0.01	0.02	0.03	0.06	0.11	0.14
maximum deposition inside the patch ( $g/m^2$ )	$30 \pm 3$	$36 \pm 2$	$41 \pm 5$	$29 \pm 3$	$32 \pm 2$	$36 \pm 3$

## 2.5 Experimental results of flow measurements

### 2.5.1 Longitudinal profiles

Each of the velocity statistics,  $\bar{u}$ ,  $\bar{v}$ ,  $u_{rms}$ ,  $v_{rms}$  and  $\sqrt{(-\bar{U}'\bar{V})}$ , was normalized by the upstream channel velocity,  $U_\infty$ . The normalized profiles collapsed into two groups, corresponding to the two patch densities  $\Phi = 2\%$  and  $\Phi = 10\%$  (Fig. 2.7 and 2.8). This shows that for a given patch density the flow field in and around the patch is self-similar, scaling upon the upstream flow rate. Approaching along the centerline of the patch ( $y = 20$  cm), the longitudinal velocity ( $\bar{u}$ ) began to decrease 1-m upstream of the leading edge for the dense patch ( $\Phi = 0.10$ , Fig. 2.7a) and 0.5 m upstream of the leading edge for the sparse patch ( $\Phi = 0.02$ , Fig. 2.7a). The deceleration in  $\bar{u}$  occurred continuously, with no distinct behavior at the leading edge ( $x = 0$ ). The deceleration in longitudinal velocity was necessarily accompanied by an increase in lateral velocity,  $\bar{v}$ , associated with the diversion of flow away from the patch (Fig. 2.7b). Within the patch ( $x > 0$ ),  $\bar{u}$  continued to decrease until the diverging flow ( $\bar{v}$  in Fig. 2.7b) ended at roughly  $x_D = 200$  cm for the dense patch and  $x_D = 400$  cm for the sparse patch. Beyond the diverging region ( $x > x_D$ ), the velocity along the centerline of the patch was uniform ( $\partial\bar{u}/\partial x = 0$ ) until the end of the patch ( $x = 10$  m) (Fig. 2.7a), and the cross-stream velocity ( $\bar{v}$ ) was zero (Fig. 2.7b).

In order to predict the length of the flow developing region ( $x_D$ ) from Eq. (2.1), the flow-blockage,  $C_D ab$ , is needed.  $C_D$  is the bulk drag coefficient for the vegetation, and it varies with stem density ( $\Phi$ ) and the stem Reynolds number,  $Re_d = \bar{u}d/\nu$ . Tanino and Nepf (2008) found the values of  $C_D$  for a random array of rigid emergent cylinders, covering the solid volume fraction  $\Phi = 0.091 - 0.35$  and  $Re_d = 25 - 685$ . Based on the values of  $C_D$  reported by Tanino and Nepf (2008) and the solid volume fraction considered here, I confirmed that  $C_D = 1$  is a reasonable simplification.  $C_D ab = 8$  and 1.6 for  $\Phi = 0.10$  and 0.02, respectively. Both cases are in the regime of high flow-blockage ( $C_D ab > 2$ ). Eq. (2.1) predicts  $x_D = 210$  cm and 320 cm for the dense and sparse patch, respectively, which are consistent with the observed lengths in Figure 2.7.

After  $x_D$ , the final interior velocity is reached,  $U_I/U_\infty = 0.02$  and 0.1 for  $\Phi = 0.10$  and 0.02, respectively (Fig. 2.7). Since both patch densities are in the regime of high flow-blockage,  $U_I/U_\infty$  can be estimated from Eq. (2.2) using the known friction coefficient of the PVC baseboards,  $C_f = 0.006$ , the drag coefficient,  $C_D = 1$ , size of the cylinder,  $d = 0.6$  cm, and the water depth,  $h = 13$  cm,

$$\frac{U_I}{U_\infty} = 0.02 \sqrt{\left(\frac{1}{\Phi} - \Phi\right)}. \quad (2.11)$$

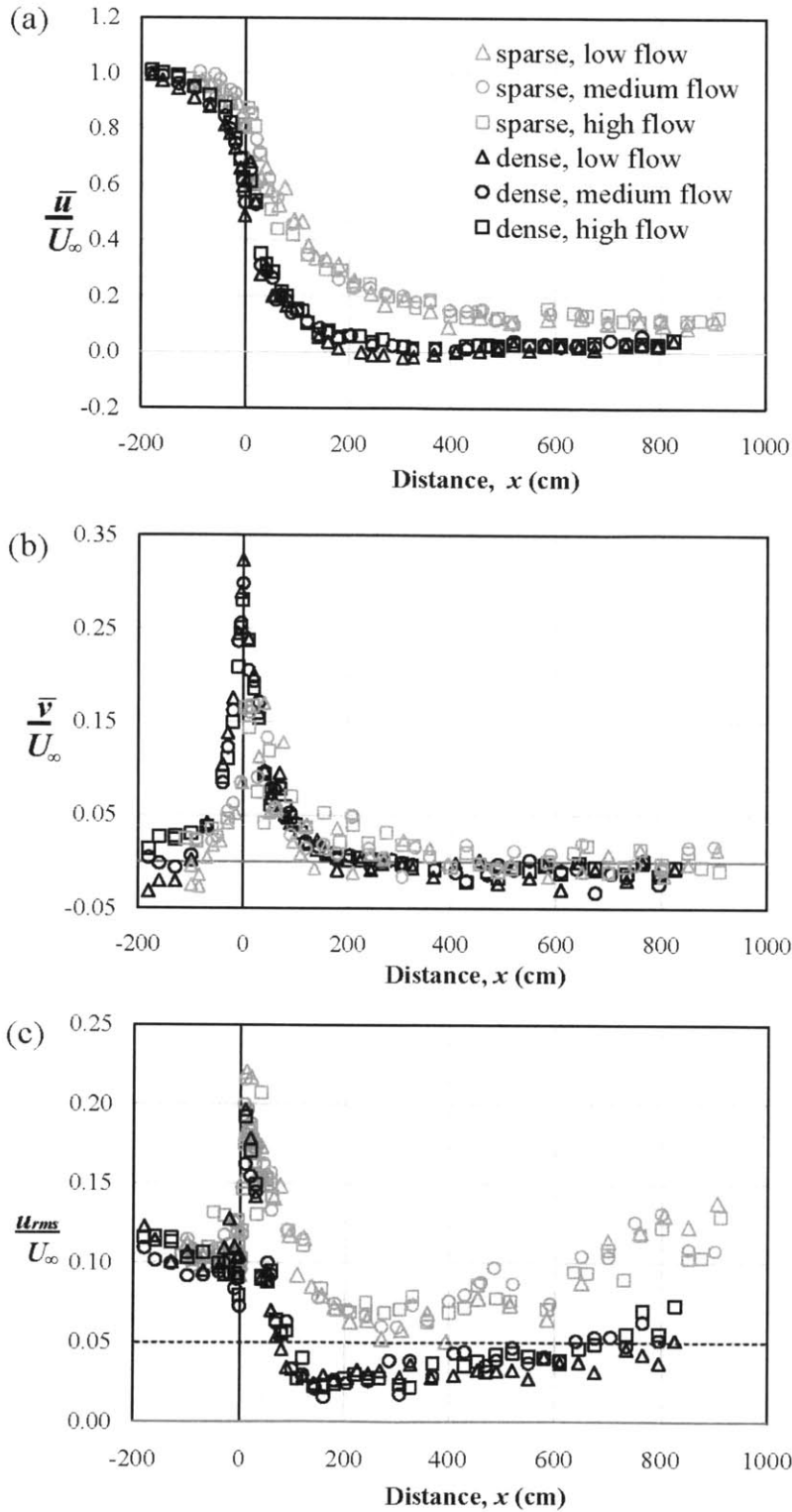


Figure 2.7 Velocity measured along the mid-patch transect at  $y=20$  cm, normalized by the upstream velocity,  $U_\infty$ . Patch extends from  $x=0$  to  $x=1000$ cm, and  $y=0$  to  $y=40$ cm. (a) Time averaged stream-wise velocity,  $\bar{u}$ . (b) Time-averaged lateral velocity,  $\bar{v}$ . (c) Stream-wise velocity fluctuation,  $u_{rms}$ . The uncertainty in each velocity measurement is  $\pm 0.1$ cm/s. The noise level is  $u_{rms}/U_\infty \approx 0.05$ .

Eq. (2.11) gives that  $U_1/U_\infty = 0.06$  and  $0.14$  for  $\Phi = 0.10$  and  $0.02$ , respectively, which are in agreement with the experimental results. The total patch length is expected to have no influence on the length of the diverging region ( $x_D$ ) and the final interior velocity ( $U_1$ ), provided that the patch is longer than  $x_D$ . For example, Zong and Nepf (2010) tested an 8-m long patch with the same patch densities and obtained similar values for  $x_D$  and  $U_1$ .

Upstream of the patch the turbulence intensity was similar to that found in an open channel flow, specifically  $u_{rms}/U_\infty \approx 0.1$  (Schlichting 1960). The turbulence levels increased sharply at the leading edge of the patch ( $x = 0$ ), even as the mean velocity decreased continuously across this zone. This region of elevated turbulence intensity is associated with the additional production of turbulence in stem wakes, and it is associated with a local region of diminished deposition, as discussed in Zong and Nepf (2010). The stem-wake production occurs for stem Reynolds number,  $Re_d = \bar{u}d/\nu$ , greater than approximately 100, although the exact threshold is dependent on the stem density (Nepf 1999). As  $Re_d$  declined with declining velocity in the patch, this source of turbulence was reduced and eventually shut off. For the dense patch, the measured turbulence intensity dropped below the noise threshold (dashed line in Fig. 2.7c) for  $x > x_D$ , implying laminar flow conditions. This is consistent with the stem-scale Reynolds numbers ( $Re_d = U_1d/\nu$ ) and the depth-scale Reynolds numbers ( $Re_h = U_1h/\nu$ ) reported in Table 2.1. In contrast, for the sparse patches  $u_{rms}/U_\infty$  remained above the noise level, indicating that some turbulence was present, consistent with the transitional Reynolds numbers reported in Table 2.1.

## 2.5.2 Lateral profiles

Lateral profiles of velocity were measured in the fully developed region of the patch,  $x > x_D$  (Fig. 2.8). The solid line at  $y = 40$  cm denotes the edge of the patch. The time-mean velocity was laterally uniform over most of the patch width, increasing toward the free stream within the distance  $\delta_v$  from the edge. The dashed lines indicate the penetration distance estimated from Eq. (2.4) using  $C_D = 1$ ,  $d = 0.6$  cm, specifically  $\delta_v = 2$  cm and  $12$  cm, for the dense and sparse patch, respectively. The estimated penetration distances do reasonably well in describing the points at which the velocity begins to increase near the edge (Fig. 2.8a), as well as the regions of elevated  $-\overline{u'v'}$  and  $u_{rms}$  within the patch (Fig. 2.8b and c). The magnitudes of the peak Reynolds stress observed near the patch edge were consistent with previous studies of vegetated shear-layers, specifically White and Nepf (2008) give the scaling,  $\sqrt{(-\overline{u'v'})_{\max}}/(U_2 - U_1) \approx 0.1$ .

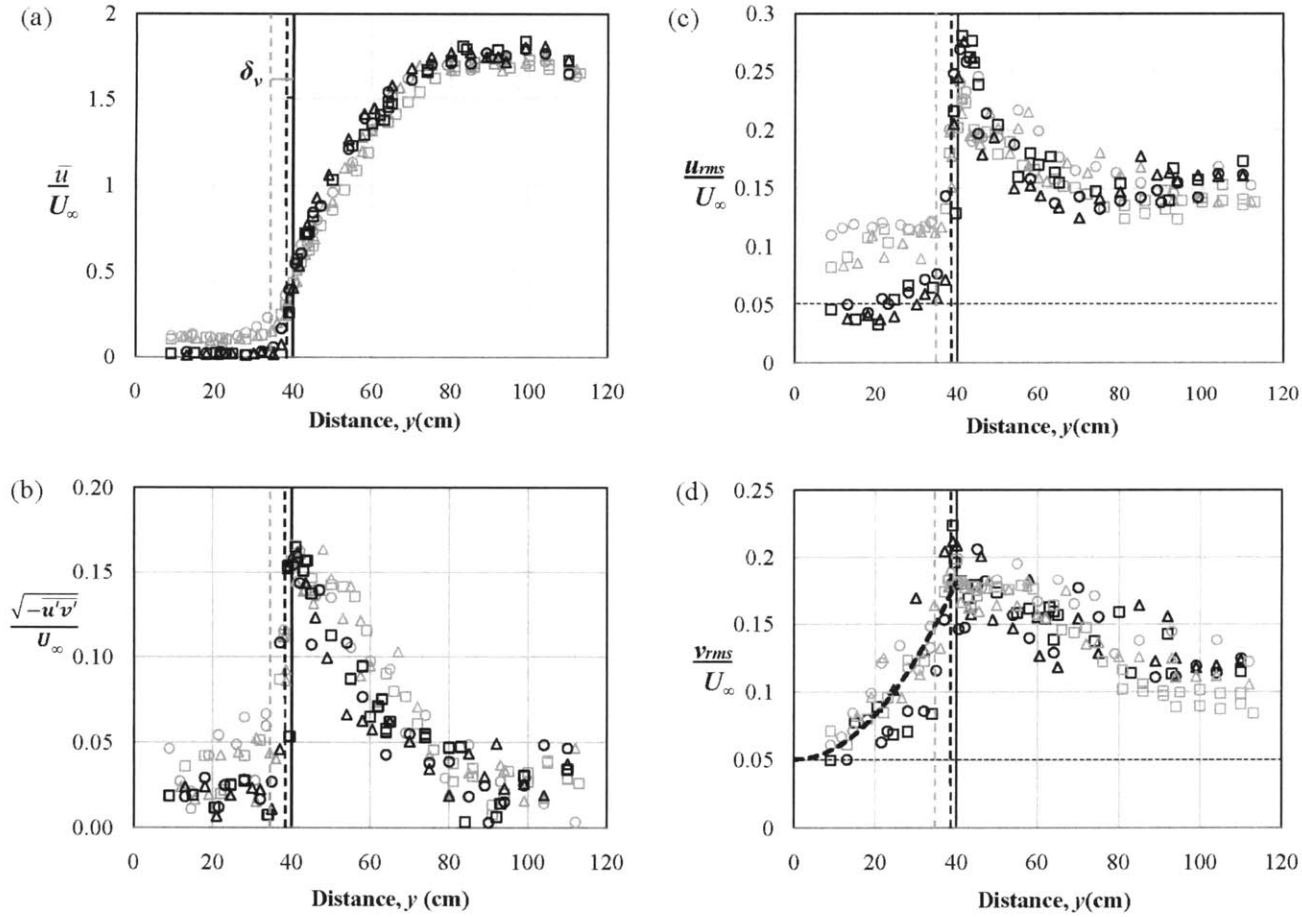


Figure 2.8 Lateral profiles of velocity statistics measured in the developed region ( $X > X_D$ ). In the sparse patch,  $X = 760$  cm for high flow rate,  $X = 800$  cm for median flow rate,  $X = 700$  cm for low flow rate. In the dense patch,  $X = 675$  cm for all flow conditions. Symbols are given in Figure 2.7. In each subplot the position of  $\delta_v$  is shown for the dense patch (black dashed line) and the sparse patch (grey dashed line). (a) Time-averaged stream-wise velocity,  $\bar{u}$ . (b) Reynolds stress,  $\sqrt{-u'v'}$ . (c) Streamwise velocity fluctuation,  $u_{rms}$ . (d) Cross-stream velocity fluctuation,  $v_{rms}$ . The dashed curve in (d) represents the shape function  $v_{rms}/U_\infty = (v_{rms}/U_\infty)_{max}(y/b)^2 + (v_{rms}/U_\infty)_{background}$ . This shape function is used as the basis for modeling the lateral dispersivity.

The shear layer extends into the open channel ( $y > b = 40$  cm) over a distance  $\delta_o \sim h/C_f$  (White and Nepf 2007 & 2008), where  $h$  is the flow depth and  $C_f$  is the bed friction. In this study, the flow depth varied only from 12 cm to 14 cm and  $C_f = 0.006$  for all cases, so the width of the shear-layer in the open channel was approximately the same for all cases, as seen in Figure 2.8a. Both mean flow ( $\bar{u}$ ) and  $u_{rms}$  were uniform in the open channel beyond the shear layer ( $y > 80$  cm). For both patch densities,  $u_{rms}/U_\infty \approx 0.15$  (Fig. 2.8c). Since  $U_2/U_\infty \approx 1.7$  (Fig. 2.8a),  $u_{rms}/U_2 \approx 0.15/1.7 \approx 0.1$ , which is typical for the open channel flow (Schlichting 1960).

Although  $u_{rms}$  and Reynolds stress were nearly uniform across the inner patch ( $y < b - \delta_v$ ), the cross-stream velocity fluctuation ( $v_{rms}$ ) was not (Fig. 2.8d). The cross-stream fluctuating velocity was maximum at the edge of the patch and decreased with distance from the edge, both into the channel and into the patch. The elevated  $v_{rms}$  is associated with an edge-wave induced by the passage of the shear-layer vortices, which is described in White and Nepf (2007). The passage of the vortex train along the flow-parallel edge of the patch generates two distinct flows, which are revealed by the time series of the streamwise and transverse velocity ( $u(t)$  and  $v(t)$ ). Time series measured in the outer patch region (Fig. 2.9a) reflect the direct impact of the vortices on turbulent flux. In this region the fluctuation of  $u(t)$  and  $v(t)$  are anti-phase, producing strong fluxes of momentum ( $\overline{u'v'} < 0$ ). In contrast, within the inner patch region ( $y = 20$  cm, Fig. 2.9b),  $u(t)$  and  $v(t)$  are  $\pi/2$  out of phase, producing no momentum flux ( $\overline{u'v'} = 0$ ). Further, the transverse velocity within the patch lags the low pressure of the passing vortex core by 90 degrees (White, 2006). These phase relationships are consistent with a pressure wave (Betchov and Criminale 1967), *e.g.* a free surface gravity wave. As described in section 2.2, the progression of vortices passing along the vegetation edge generates a wave response within the patch that is predominantly manifest in an oscillating lateral motion with a frequency fixed by the frequency of vortex passage, and the maximum lateral velocity lagging the vortex core by 90 degrees.

Finally, note that for  $x > x_D$ , the  $u_{rms}/U_\infty$  level in the sparse patches increased longitudinally (Fig. 2.7c), even as the mean velocity remained constant. The increase in  $u_{rms}$  is likely associated with the edge-wave. As the vortices initially grow longitudinally (Fig. 2.2), the forced wave also grows in strength, leading to the observed increase of  $u_{rms}/U_\infty$  with distance.

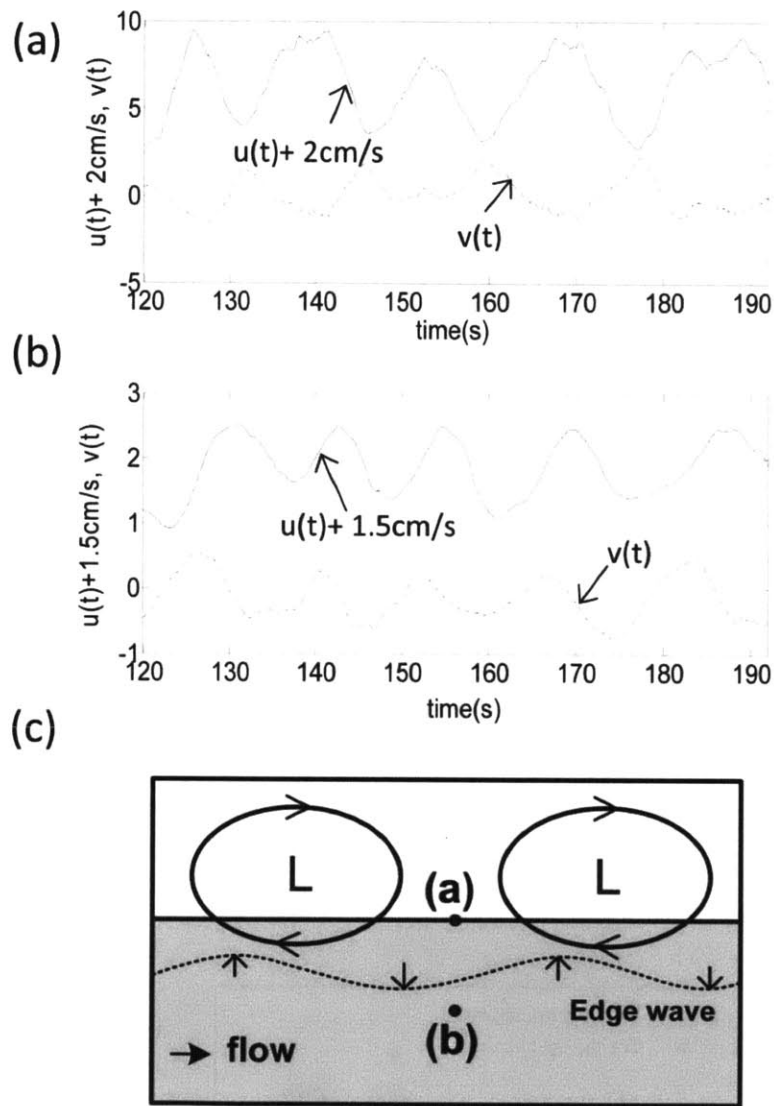


Figure 2.9 Time series of streamwise ( $u$ , solid line) and transverse ( $v$ , dashed line) velocity components at  $x = 735$  cm, and (a) at the flow-parallel edge (pt (a):  $y = 40$ cm), and (b) in the middle of the patch (pt (b):  $y = 20$ cm). (c) Location of measurements (a) and (b), and schematic of edge-wave generation.

## 2.6 Experimental results of deposition measurements

Figure 2.10 compares the spatially-averaged net deposition measured within the patch and within the open channel for each case. For the open-channel the average was taken using the points beyond the shear-layer ( $y > 80$  cm), where the velocity ( $\bar{u} = U_2$ ) and the observed deposition was laterally uniform. For the in-patch deposition, the average was taken using all points within the patch. In the open channel (open bars in Fig. 2.10) the net deposition decreased as the flow rate increased. This is consistent with expectations. The net deposition is equal to the deposition minus the resuspension, and resuspension is expected to increase with the flow rate. Further, in nearly all cases the deposition in the patch was higher than the deposition in the channel. This is also consistent with deposition limited by resuspension, because in all cases the velocity in the patch was significantly lower than that in the open channel ( $U_1 < U_2$ , Table 2.1). The difference between in-patch and open channel deposition increased with increasing patch density, because the velocity difference between these regions increased with patch density (Table 2.1). There was, however, one important exception. For the lowest flow condition in the dense patch, the spatially-averaged deposition in the patch was, within uncertainty, the same as that in the open channel. At first, this seems surprising, because the flow speed in the patch ( $U_1 = 0.1$  cm/s) was significantly less than that in the open channel ( $U_2 = 9.0$  cm/s). However, this result can be explained by considering when deposition is limited by the supply of suspended sediment to the patch, rather than by resuspension. As discussed below, for the dense patch under the lowest flow condition the advection distance,  $\chi_a = 1.2$  m, was much shorter than the patch length, 10m, so that significant regions of this patch were supply limited, *i.e.* deposition was limited by supply.

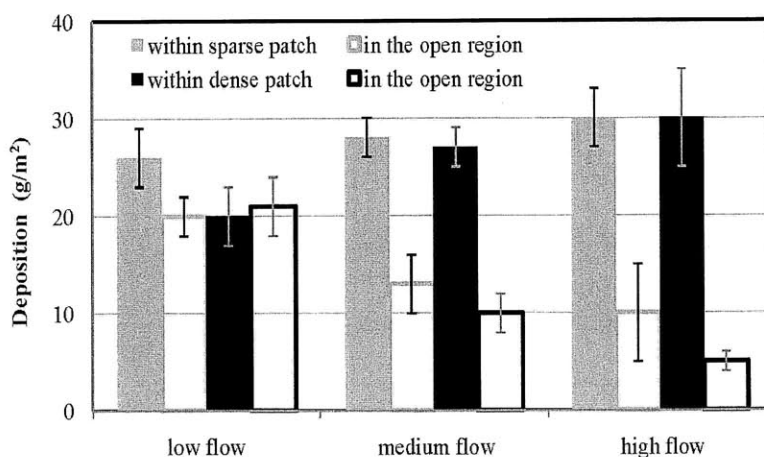


Figure 2.10 Spatially-averaged deposition within the patch and in the open channel. The open channel average only includes measurements beyond the shear layer where  $\bar{u} = U_2$ , specifically from  $y = 100$ cm and  $x = 5$ m, 5.5m, 6m, 6.5m and 7m. The in-patch average includes all measurements made within the patch. Vertical bars indicate the standard error.

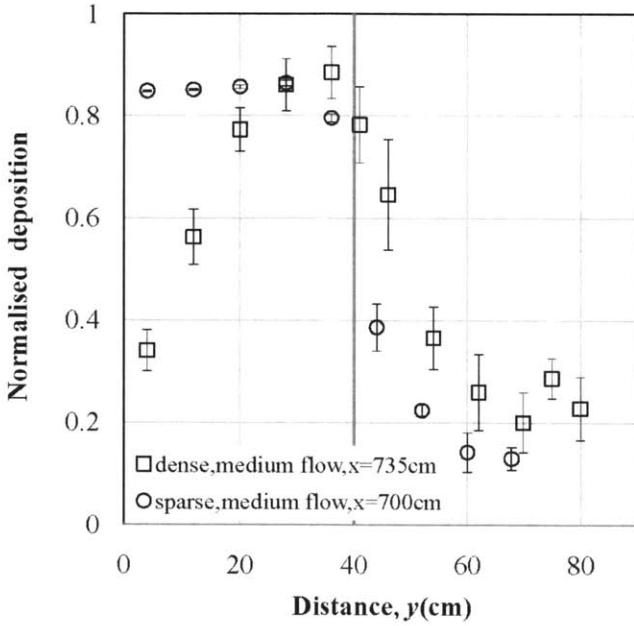


Figure 2.11 Net deposition observed for median flow condition ( $U_\infty = 9.0$  cm/s) at  $x = 700$  cm in the dense patch ( $\square$ ) and  $x = 735$  cm in the sparse patch ( $\circ$ ). The patch is  $0 < y < 40$  cm.

To illustrate the role of the advection length-scale,  $\chi_a$ , or more specifically the transition distance from the leading edge,  $\chi_D + \chi_a$ , consider the lateral patterns of deposition observed at positions both greater than and less than the transition distance. For each case shown in Figures 2.11, 2.12 and 2.13, the deposition was normalized by the maximum deposition observed inside the patch (Table 2.1). First, consider the deposition pattern observed at comparable longitudinal positions ( $x = 700$  cm and 735 cm), and at comparable channel speeds ( $U_\infty = 9.0$  cm/s), but within patches of different stem density (Fig. 2.11). The difference in patch density produced different patch velocities,  $U_T = 0.2$  and 1.1 cm/s in the dense and sparse patch, respectively. This led to different advection length-scales,  $\chi_a = 260$  cm (dense) and 1430 cm (sparse), which corresponded to a different transition distance from the leading edge of  $\chi_D + \chi_a = 460$  cm (dense) and 1830 cm (sparse). For the sparse case shown in Figure 2.11 the measured pattern of deposition was laterally uniform over the patch width except for the point closest to the flow-parallel edge. Recall that the flow field is also laterally uniform within the patch. Together, these observations suggest that the particle delivery to this region is dominated by longitudinal advection. This is consistent with the advection length scale, *i.e.* particle delivery is dominated by the advection from the leading edge if  $x \ll \chi_D + \chi_a$ , as is the case for the sparse patch shown in Figure 2.11. The reduced deposition near the flow-parallel edge is probably due to the enhanced turbulence at the patch edge, associated with the shear-layer vortices. Now consider the dense patch, for which the deposition was not uniform across the patch width (Fig. 2.11). The deposition was highest near the flow parallel edge and decreased with the distance into the patch. In this case,  $x = 735$  cm  $>$   $\chi_D + \chi_a = 460$  cm, which indicated that a large fraction of

particles supplied by advection across the leading edge had been lost to deposition upstream of this point, and the supply of particles by diffusion from the lateral edge should be important here. Indeed, the deposition pattern was consistent with particle supply dominated by diffusion from the flow parallel edge.

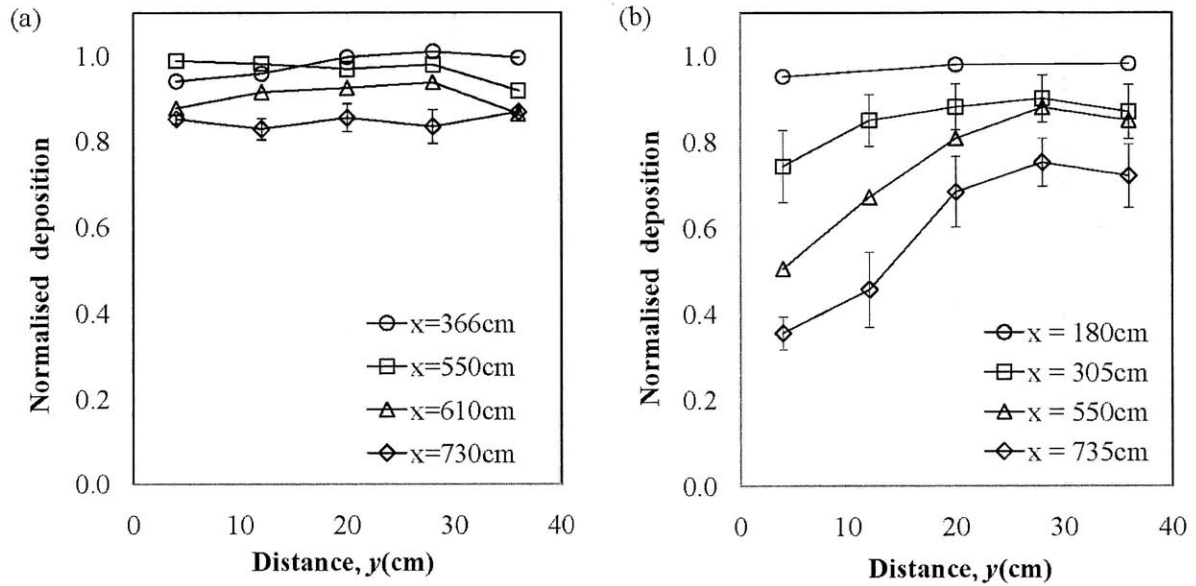


Figure 2.12 Net deposition within the patch,  $0 < y < 40$  cm. (a) In the sparse patch with low flow condition ( $U_\infty = 5.0$  cm/s), deposition measured at  $x = 366, 488, 610$  and  $730$  cm. (b) In the dense patch with high flow condition ( $U_\infty = 11.6$  cm/s), deposition measured at  $x = 180, 305, 550$  and  $735$  cm.

Now consider how the lateral pattern of deposition evolves longitudinally within a single patch. First, consider the sparse patch under the low flow condition (Fig. 2.12a), for which the transition distance is longer than the entire patch length,  $x_D + x_a = 1120$  cm  $> l = 1000$  cm. The deposition was uniform across the patch width at every measurement position, which is consistent with particle supply by longitudinal advection that is laterally uniform, as discussed above. The decline in deposition with increasing  $x$  was due to the loss of suspended sediment to upstream deposition within the patch. To contrast this, consider the dense patch under the highest channel flow (Fig. 2.12b), for which the transition distance falls near the mid-length of the patch, specifically  $x_D + x_a = 620$  cm  $< l = 1000$  cm. The deposition near the leading edge ( $x = 180$  cm  $< x_D + x_a = 620$  cm) was uniform across the patch, consistent with particle supply by advection from the leading edge. Farther downstream (increasing  $x$ ), the deposition pattern shifted to a laterally non-uniform pattern, with higher deposition near the flow parallel edge, which is consistent with particle delivery into the patch by lateral dispersion from the edge. The non-uniformity becomes pronounced at the third transect,  $x = 550$  cm, consistent with the estimated transition distance. An

important point to recall about this case is that the flow within the patch was laminar, so that the lateral flux due to turbulent diffusion should be zero, and the contribution from molecular diffusion would be negligible over the settling time-scale. However, the deposition pattern indicates that lateral flux had occurred. I propose that the motion associated with the edge wave provided another mechanism for lateral flux of particles into the patch. This is explored further below.

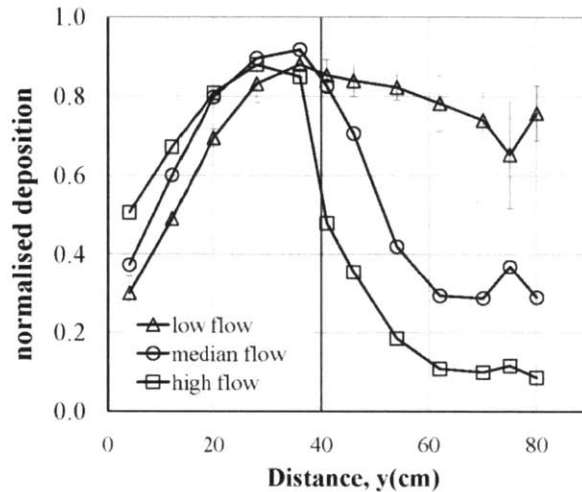


Figure 2.13 Net deposition measured at  $x = 550$  cm in the dense patch for the three flow conditions. The patch is  $0 < y < 40$  cm.

Finally, consider the unusual result revealed in Figure 2.10, that the dense patch under the lowest channel flow experienced an average deposition comparable to that in the channel. Three deposition profiles measured in the dense patch, at the same position ( $x = 550$  cm), but under the three different flow conditions are shown in Figure 2.13. The deposition across the patch width was similar for all flow conditions, with maximum deposition near the flow-parallel edge. As the upstream channel flow,  $U_\infty$ , decreased, the deposition in the patch decreased only slightly, while the deposition in the open region increased significantly. The trend in the open region is consistent with net deposition limited by resuspension, *i.e.* as the open channel velocity decreased, the resuspension decreased, and the net deposition increased. Within the patch, however, the deposition was supply limited. For the lowest channel flow, the supply-limited conditions within the dense patch limited the average patch deposition to values comparable to that observed in the open channel.

## 2.7 Using model to examine the lateral dispersion of particles

The numerical model introduced in Section 2.3 is used to explore a new model for lateral dispersion. I previously assumed a homogeneous diffusivity for the inner patch,  $D_y = D_{t,i}$ , based on turbulence generation within stem wakes (Eq. 2.5). The model predicted suspended sediment concentration,  $C(x,y)$ . Assuming no resuspension in the patch, the net deposition,  $m$ , is related directly to  $C$ , specifically  $m(x,y) = w_s C(x,y) T$ , with  $T$  the duration of the experiment. First, compare the measured deposition profiles to those produced by the model with a constant diffusivity  $D_{t,i}$ , (Fig. 2.4). Specifically, consider the profile at  $x = 550$  cm in Figure 2.12b, which has a dimensionless distance  $(x - x_D)/X_a = 0.83$ . This distance is close to  $(x - x_D)/X_a = 1$ , for which a modeled profile is shown in Figure 2.4b. The lateral extent of the measured deposition (Fig. 2.12b) is larger than that produced by the model (Fig. 2.4b), suggesting that the lateral flux of particles was greater than turbulent diffusion alone. In addition, the flow conditions in the dense patch were laminar, so that Eq. (2.5) and the modeled result would at best be an upper bound for the impact of stem-wake diffusivity. Also, note that the modeled profile is convex, but the measured profile is concave. The concave shape suggests that  $D_y$  is larger near the patch edge and decreasing away from that edge. The above comparison between observed and modeled profiles suggests that another mechanism, in addition to turbulent diffusion, transports particles laterally into the patch, and that its dispersivity is highest near the flow parallel edge and decreasing into the patch. The edge wave, because it generates oscillating lateral velocity (Fig. 2.8d), could provide another mechanism for lateral flux into the patch. Further, the velocity scale associated with the edge wave is highest at the patch edge and decreasing into the patch. A reasonable fit to the profile of  $v_{rms}$  is  $v_{rms} = v_{rms,max}(y/b)^2 + v_{rms,background}$ , which is shown as a dashed line in Figure 2.8d. If  $v_{rms}$  sets the velocity scale for the lateral particle flux, then the dispersion coefficient would have a similar form (Fig. 2.14a), specifically,

$$D_y = D \left( \frac{y}{b} \right)^2 + D_{t,i} \quad (2.12)$$

The first term,  $D(y/b)^2$ , captures the contribution from the edge wave, and the second term,  $D_{t,i}$ , represents the contribution from background turbulence associated with stem wakes.

The numerical model introduced above was run again using parameter values from the current study, specifically  $U_t$ ,  $D_{t,i}$ , and  $\delta_v$  reported in Table 2.1. The coefficient  $D$  was adjusted to obtain the best fit between measured and simulated deposition. Figure 2.14 compares the model deposition (line) with the observed deposition (circles) for the dense patch under the three flow conditions. The modeled profiles capture the concave shape observed in the measured profiles. In addition, the fitted dispersion coefficients (listed in each subplot) were much greater than the turbulent diffusivity,  $D_{t,i} = 0.01$  to  $0.03$  cm<sup>2</sup>/s (Table 2.1). Finally, the fitted coefficient,  $D = 1.5$  cm<sup>2</sup>/s,  $1.9$  cm<sup>2</sup>/s and  $2.1$  cm<sup>2</sup>/s, increased with flow speed  $U_\infty =$

## 2.7 Using model to examine the lateral dispersion of particles

The numerical model introduced in Section 2.3 is used to explore a new model for lateral dispersion. I previously assumed a homogeneous diffusivity for the inner patch,  $D_y = D_{t,i}$ , based on turbulence generation within stem wakes (Eq. 2.5). The model predicted suspended sediment concentration,  $C(x,y)$ . Assuming no resuspension in the patch, the net deposition,  $m$ , is related directly to  $C$ , specifically  $m(x,y) = w_s C(x,y)T$ , with  $T$  the duration of the experiment. First, compare the measured deposition profiles to those produced by the model with a constant diffusivity  $D_{t,i}$ , (Fig. 2.4). Specifically, consider the profile at  $x = 550$  cm in Figure 2.12b, which has a dimensionless distance  $(x - x_D)/x_a = 0.83$ . This distance is close to  $(x - x_D)/x_a = 1$ , for which a modeled profile is shown in Figure 2.4b. The lateral extent of the measured deposition (Fig. 2.12b) is larger than that produced by the model (Fig. 2.4b), suggesting that the lateral flux of particles was greater than turbulent diffusion alone. In addition, the flow conditions in the dense patch were laminar, so that Eq. (2.5) and the modeled result would at best be an upper bound for the impact of stem-wake diffusivity. Also, note that the modeled profile is convex, but the measured profile is concave. The concave shape suggests that  $D_y$  is larger near the patch edge and decreasing away from that edge. The above comparison between observed and modeled profiles suggests that another mechanism, in addition to turbulent diffusion, transports particles laterally into the patch, and that its dispersivity is highest near the flow parallel edge and decreasing into the patch. The edge wave, because it generates oscillating lateral velocity (Fig. 2.8d), could provide another mechanism for lateral flux into the patch. Further, the velocity scale associated with the edge wave is highest at the patch edge and decreasing into the patch. A reasonable fit to the profile of  $v_{rms}$  is  $v_{rms} = v_{rms,max}(y/b)^2 + v_{rms,background}$ , which is shown as a dashed line in Figure 2.8d. If  $v_{rms}$  sets the velocity scale for the lateral particle flux, then the dispersion coefficient would have a similar form (Fig. 2.14a), specifically,

$$D_y = D \left( \frac{y}{b} \right)^2 + D_{t,i} \quad (2.12)$$

The first term,  $D(y/b)^2$ , captures the contribution from the edge wave, and the second term,  $D_{t,i}$ , represents the contribution from background turbulence associated with stem wakes.

The numerical model introduced above was run again using parameter values from the current study, specifically  $U_s$ ,  $D_{t,i}$ , and  $\delta_v$  reported in Table 2.1. The coefficient  $D$  was adjusted to obtain the best fit between measured and simulated deposition. Figure 2.14 compares the model deposition (line) with the observed deposition (circles) for the dense patch under the three flow conditions. The modeled profiles capture the concave shape observed in the measured profiles. In addition, the fitted dispersion coefficients (listed in each subplot) were much greater than the turbulent diffusivity,  $D_{t,i} = 0.01$  to  $0.03$  cm<sup>2</sup>/s (Table 2.1). Finally, the fitted coefficient,  $D = 1.5$  cm<sup>2</sup>/s,  $1.9$  cm<sup>2</sup>/s and  $2.1$  cm<sup>2</sup>/s, increased with flow speed  $U_\infty =$

5.0, 9.0, 11.6 cm/s, respectively, consistent with  $V_{rms}$ , which also scales with the channel flow speed (Fig. 2.8).

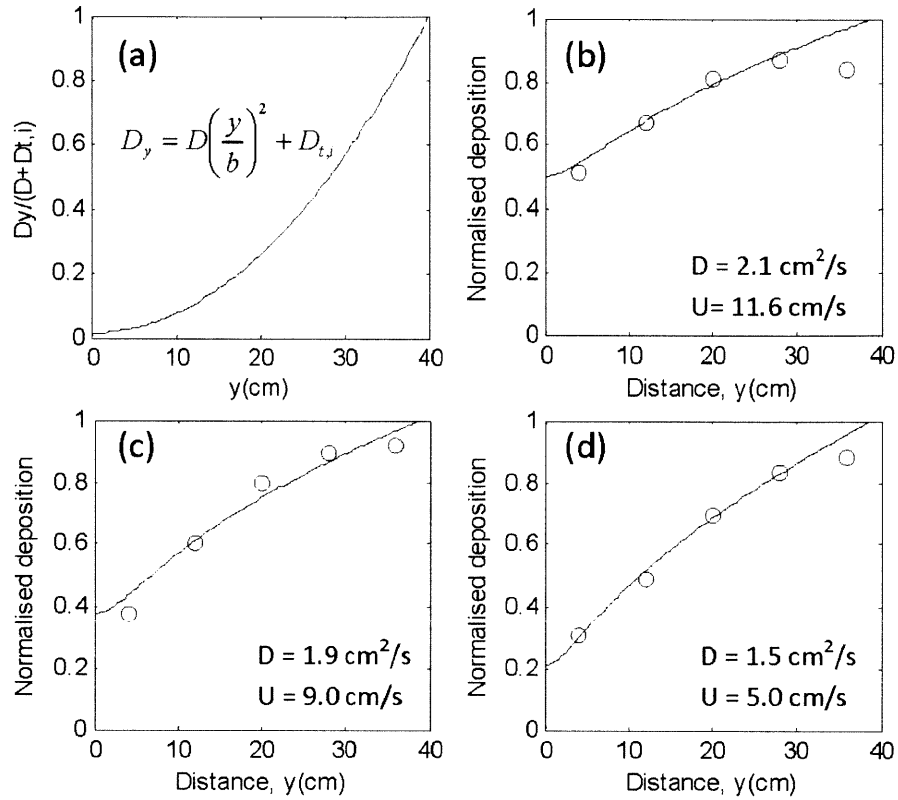


Figure 2.14 (a) Dispersivity model used for simulated results,  $D_y = D(y/b)^2 + D_{t,i}$ . Measured ( $\circ$ ) and simulated (solid line) profiles of deposition at  $x = 550 \text{ cm}$  in the dense patch for (b) high flow; (c) medium flow; and (d) low flow.

## 2.8 Conclusion

This chapter describes the flow structure and the spatial pattern of deposition in a finite patch of vegetation at the sidewall of a channel (*i.e.* a partially vegetated channel). For each patch density, the flow field was self-similar when scaled with the channel velocity,  $U_\infty$ . Along the centerline of the patch, the flow began to decelerate upstream of the patch and continued to decelerate until the distance  $x_D$  past the leading edge. Beyond  $x_D$ , the shear-layer vortices developed at the flow-parallel interface and penetrated into the patch a distance,  $\delta_v$ . The vortices enhanced the transport of particles into the patch by increasing the turbulent flux in the outer patch region ( $y > b - \delta_v$ ), and also by inducing an edge wave that enhanced lateral motion across the patch. In addition to lateral flux across the flow-parallel edge, suspended particles were also supplied to the patch by mean flow advection across the leading edge. The relative contribution from these two supplies can be described by the length-scale,  $x_D + x_a$ . For  $x < x_D + x_a$ , the supply is dominated by mean advection. Because the flow field was laterally uniform within the patch, the net deposition in this region was also laterally uniform. Beyond  $x_D + x_a$  the supply is dominated by lateral flux across the flow-parallel edge, and the net deposition was highest near that edge and decreased toward the patch interior. The lateral flux from the flow-parallel edge consisted of two mechanisms: turbulent diffusion and edge-wave dispersion. Both mechanisms scale with the channel flow,  $U_\infty$ . The dispersivity estimated by fitting model simulations to the observed net deposition suggested that for the conditions consider here the dispersion associated with the edge-wave-oscillations in lateral velocity was more important than the turbulent diffusion in transporting particles into the patch. Finally, if the patch is longer than the distance  $x_D + x_a$  and wider than  $\delta_v + \delta_{max}$ , then net deposition within some regions of the patch will be supply limited and some interior regions may experience zero net deposition.

The experimental results show that the deposition is not evenly distributed in a vegetated river bank, with low deposition at the leading edge,  $0 < x < x_D$ , (due to high turbulence level) and at the locations where  $x > x_D + x_a$  and  $y < b - \delta_v - \delta_{max}$  (due to the limit particle-supply), high deposition close to the flow-parallel edge of the patch. These results suggest that there might be some heterogeneity in stem density, nutrient concentration and animal species within the vegetated bank. The region with high deposition can have more vegetation growing and therefore low nutrient concentration.

## Chapter 3

# Wake structure of a finite patch of vegetation in a channel

### 3.1 Introduction

Cylinder arrays that fill the entire flume width have been used to estimate a bulk drag coefficient, and study the diffusion and dispersion within the array (*e.g.* Nepf 1999; Tanino and Nepf 2008; Sharpe and James 2006). White and Nepf (2007, 2008) studied the flow structure in a channel-vegetated-bank system and Chapter 2 describes the deposition pattern in the vegetated bank. However, only a few projects have considered finite patches of vegetation, which have length and width scales much smaller than the channel width. Yet, this configuration is common in the field (*e.g.* Sand-Jensen and Pedersen 2008).

In this chapter, the flow structure associated with a finite patch of vegetation located in the middle of the channel is examined. Previous studies, Ball et al. (1996), Takemura and Tanaka (2007), also investigated the flow passing through a group of cylinders (*i.e.* a model of vegetation patch). This finite patch of vegetation can be considered as a porous obstruction. Castro (1971), Huang and Keffer (1996) investigated the wake structure of a porous plate. Despite using different shapes and sizes for the porous body, these studies showed that the wake behind a porous obstruction is different from that behind a solid

body. In particular, they all observed that a steady wake region formed directly behind the porous obstruction, and the von-Karman vortex street originated further downstream in the wake. Castro (1971) found that, for high porosity, the vortices were never formed. In this Chapter, a two-dimensional, circular porous obstruction (or a patch of vegetation) is constructed from an array of circular cylinders. The wake structure observed for circular patches with solid volume fraction ( $\Phi$ ) of 100%, 9.6% and 2.6% are shown in Figure 3.1a, b and c, respectively. Dye was injected at the two sides of the patch. Behind the solid body (Fig. 3.1a), the dye is swept into the familiar von-Karman vortex street immediately downstream of the obstruction. In contrast, for the porous cases (b) and (c), there is a region directly behind the porous body, which represents the steady wake region, in which the dye moved along straight lines with no lateral motion. That is, the single vortex street did not form until some distance downstream. As solid volume fraction decreases (*i.e.* porosity increases) from b to c, the initiation of the vortex street occurs further downstream, and the lateral extent of the vortex street became smaller, *i.e.* suggesting that the strength of the vortices in the street has decreased.

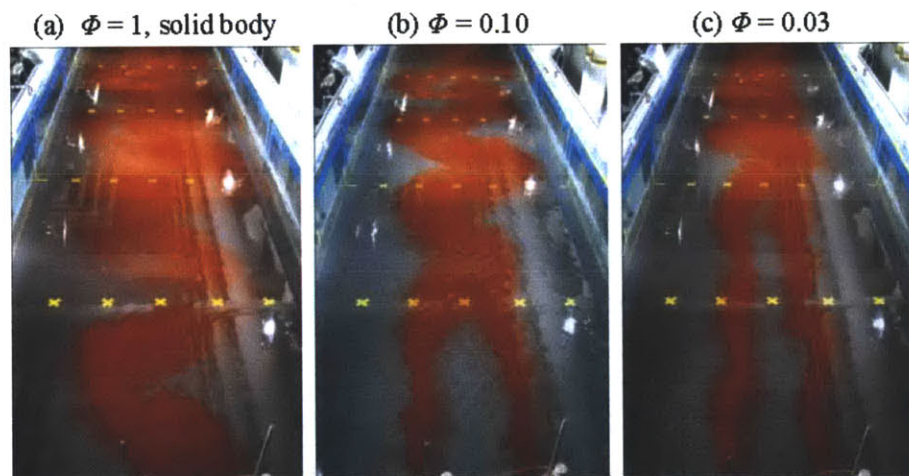


Figure 3.1 Pictures of the two-dimensional wakes behind three porous obstructions of diameter  $D = 22\text{cm}$ , and with different solid volume fraction ( $\Phi$ ). Flume is 1.2m wide and the obstruction is placed in the middle of the flume. Flow is from bottom to top of the image. The rows of crosses mark off 1m intervals from the upstream end of the patch. The lateral distance between two markers in the same row is 20cm.

A schematic sketch of the flow field around a patch is shown in Figure 3.2. The uniform flow approaching the patch starts to divert due to the drag force imposed by the patch. Flow continues diverting within the patch, resulting in a velocity deficit at the downstream end of the patch. This low flow continues in the near wake ( $U_1$ , note that  $U_1$  in this chapter has a different definition from  $U_1$  used in Chapter 2) and there is no transverse velocity, which corresponds to the clear region shown in Figure 3.1b & c. After some distance downstream the wake oscillation starts (*i.e.* the vortex street forms). The region

from the downstream end of the patch to the starting point of the wake oscillation is called the steady wake region, defined in Ball et al. (1996). For a solid body, the steady wake region is absent and the wake oscillation occurs immediately behind the body, as shown in Figure 3.1a. The steady wake is a unique and important feature of the porous body, which might affect the mass transport in the wake.

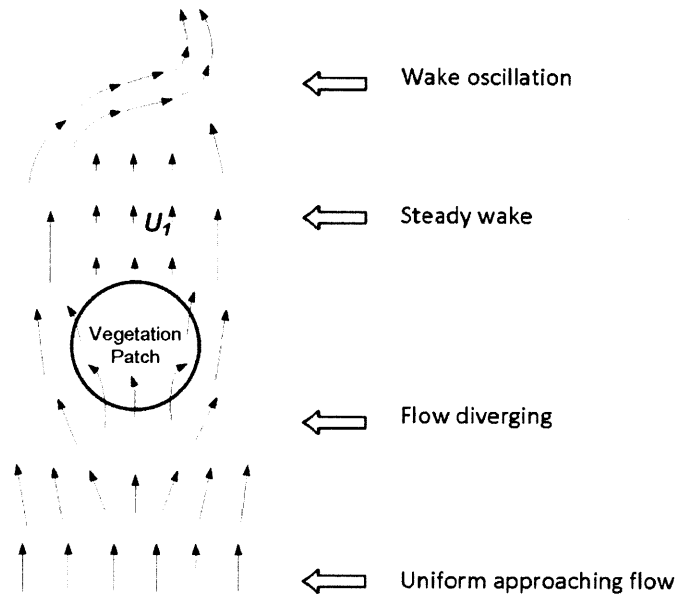


Figure 3.2 Schematic sketch of the flow field around a circular patch of vegetation, based on Fig. 5 in Ball et al. (1996). The low velocity in the near wake is  $U_1$ .

A base bleed behind a solid body creates a similar steady wake. Base bleed is the injection of flow from the trailing edge of the body into the wake. Wood (1967) used a two-dimensional aerofoil model, with a streamlined leading part and a blunt trailing edge. The base bleed flow was uniformly distributed over the trailing edge of the body, while the high velocity flow passing around the body. Wood (1967) observed that base bleed caused the vortices to form further from the body. As the bleed flow increased, vortex formation was moved to further downstream.

The above studies have all shown the presence of the steady wake region behind a porous obstruction but did not discuss the method of predicting its length from the flow condition. In this study, detailed velocity measurements and flow visualization are used to study the characteristics of the wake behind a model of a vegetation patch, in particular, I examine the length of the steady wake region and the flow velocity in the steady wake. Comparisons with the wake behind a solid body and the previous studies will also be discussed.

## 3.2 Experiment methods

Experiments were conducted in the same flume as described in Chapter 2. Circular porous obstructions were constructed with circular cylinders of diameter  $d = 0.6$  cm that extended from the bed through the water surface and were set in a staggered arrangement (Fig. 3.3a). The patches were placed at the center of the flume, beginning 3 m from the start of the test section. Individual cylinders were held in place by perforated PVC baseboards that extended over the entire bed of the flume. The bottom friction coefficient is  $C_f = 0.006$ . Three patch sizes were tested, with diameters of  $D = 12, 22$  and  $42$  cm. This study considered patches with  $\Phi = 0.03 - 0.36$  and also  $\Phi = 1$ , *i.e.* a solid obstruction (see Table 3.1). The  $x$ -axis is in the flow direction and  $y$ -axis is in the cross-stream direction.  $x = 0$  is at the leading edge of the patch and  $y = 0$  is at the flow-parallel centerline through the patch (Fig. 3.3b).

A constant upstream channel velocity was used,  $U_\infty = 9.8 \pm 0.5$  cm/s. A weir at the downstream end of the test section controlled the water depth,  $h = 13.3 \pm 0.2$  cm. Chen and Jirka (1994) showed that the vortex street behind a solid body in shallow water could be suppressed by bed friction, if the stability parameter  $S_{shallow} = C_f D / h$  was greater than 0.2. In our experiment  $S_{shallow} = 0.019, 0.01$  and  $0.005$  for patch diameter  $D = 42$  cm,  $22$  cm and  $12$  cm, respectively, which are all well below the critical value. Therefore our cases are not in the regime of shallow wakes defined by Chen and Jirka (1994).

To characterize the flow field, velocity measurements were taken using a Nortek Vectrino ADV. The measuring technique of ADV is also described in Chapter 2. Longitudinal transects were made through the centerline of the circular patch ( $y = 0$ ) and along the edge of the patch ( $y = D/2$ ), shown in Figure 3.3b. The longitudinal profiles started 1 m upstream of the patch ( $x = -1$  m) and extended 5 to 9 m downstream of the patch, depending on the patch size. No velocity measurements were made within the patch. In addition, lateral profiles were taken at several positions behind the patch. Due to the symmetry about the centerline ( $y = 0$ ), the lateral profiles were only made across half of the flume width (from the centerline to a sidewall, Fig. 3.3b). In order to compare the flow fields of a porous body and a solid body, waterproof contact paper was wrapped around the circumference of the porous body, creating a solid body of the same diameter. Similar velocity transects were made for the solid obstruction. Instantaneous records of cross-stream velocity,  $v$ , were used to find the velocity spectrum,  $S_{vv}$ .

Flow visualization was conducted in the flume. Red dye was injected at the outermost edges of the circular body (Fig. 3.3a) with a constant flow rate which matches to the ambient flow rate. The duration of injection was 2 min. The camera was positioned above the flume in order to capture the 6-m region directly behind the patch. Pictures were taken at 2 s intervals for 1 min duration and were post-processed using a Photoshop software in order to enhance the color of the dye. Tape was used to mark positions at

50 cm intervals in the  $x$ -direction and 20 cm intervals in the  $y$ -direction. Grids determined by these markers were superposed onto the pictures.

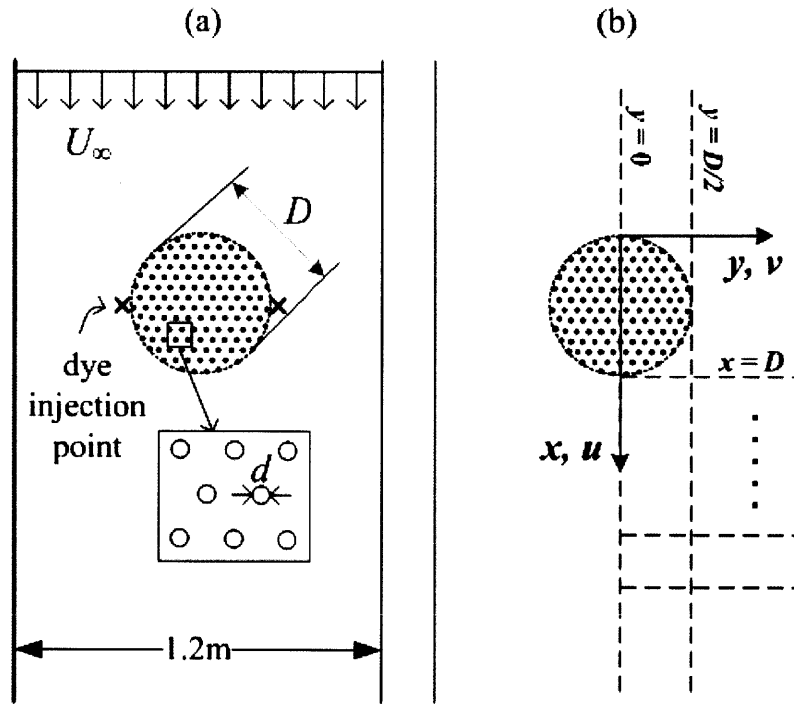


Figure 3.3 Experiment setup. (a) Patch configuration and dye injection point; (b) Longitudinal and lateral transects of velocity measurements.  $x=0$  is at the upstream edge of the patch,  $y=0$  is at the centerline of the patch.

Table 3.1 Summary of parameters. Numbers in brackets are the uncertainties of the parameters.

$D$ (cm)	42	42	42	22	22	22	22	22	22	12	12
$a$ (cm <sup>-1</sup> )	-	0.20	0.06	-	0.77	0.29	0.20	0.09	0.06	0.20	0.07
$\Phi$	1(Solid)	0.10	0.03	1(Solid)	0.36	0.14	0.10	0.05	0.03	0.10	0.04
$U_\infty$ (cm/s) $\pm 0.1$ cm/s	9.8	9.7	9.6	9.8	9.7	9.7	9.9	9.6	9.8	9.8	9.8
$U_1$ (cm/s) $\pm 0.1$ cm/s	0	0.5	5.0	0	0	0.3	0.3	3.8	5.8	0.7	5.6
$U_2$ (cm/s) $\pm 0.3$ cm/s	15.1	15.0	13.0	13.1	13.0	12.8	13.0	12.1	11.6	11.0	10.6
$U_1/U_2$	0	0.03	0.38	0	0	0.02	0.02	0.31	0.5	0.06	0.53
$V_{rms,max}$ (cm/s) $\pm 0.1$ cm/s	6.1	4.7	1.3	7.0	6.0	3.7	3.3	1.6	1.0	2.2	0.8
$L_1$ (cm) from centerline profile of $\bar{u}$	0	110 (10)	260 (10)	0	0	70 (5)	63 (5)	130 (10)	178 (10)	55 (5)	80 (5)
$L_2$ (cm) from centerline profile of $\bar{u}$	140 (10)	170 (20)	400 (30)	65 (5)	90 (5)	90 (15)	85 (15)	175 (30)	200 (20)	95 (15)	140 (15)
$L_{1,dye}$ (cm) from flow visualization	*	90 (10)	310 (20)	0	0	45 (5)	65 (5)	120 (10)	160 (10)	45 (5)	110 (20)
$L_1$ (cm) from Eq.(3.3)	0	120 (30)	245 (65)	0	0	60 (15)	60 (15)	110 (30)	170 (45)	35 (10)	100 (30)
Position of $V_{rms,max}$ (cm) measured from $x=D$	53 (5)	168 (5)	408 (20)	18 (5)	23 (5)	98 (5)	98 (10)	208 (10)	328 (20)	83 (5)	208 (20)
$St_D = f_D D/U_2$ ( $\pm 0.02$ ) ( $f_D$ from Spectrum, $S_{vv}$ )	0.20	0.20	0.24	0.16	0.17	0.17	0.16	0.17	0.18	0.16	0.14
$St_D$ ( $\pm 0.02$ ) ( $f_D$ from Flow Visual.)	*	0.20	-	0.17	0.17	0.17	0.17	0.20	-	0.18	-

\*no flow visualization - vortex street not distinct in flow visualization

### 3.3 Results of the flow field

#### 3.3.1 Mean and turbulent velocity profiles

For both the solid and porous obstructions, the streamwise velocity ( $\bar{u}$ ), measured along the flow-parallel centerline ( $y = 0$ ), begins to decrease approximately one diameter upstream of the patch (Fig. 3.4 and 3.5), consistent with scaling arguments presented in Rominger and Nepf (2011). For the porous patches the velocity continues to decelerate after entering the patch (Fig. 3b and c, 4b and c), as shown by the fact that the velocity measured at the end of the patch ( $x = D$ ) is lower than the velocity entering the patch ( $x = 0$ ). Therefore, flow diversion continues within the patch. Because of the centerline symmetry, the mean transverse velocity is zero at  $y = 0$ . However, the diverging flow is revealed by the transverse velocity,  $\bar{v}$ , measured at the outermost edge of the patch, along a transect  $y = D/2$ . The region of positive  $\bar{v}$  represents the flow diversion away from the patch (Fig. 3.4 and 3.5).

Behind the solid obstruction the wake contains a recirculation zone, shown by the reversed flow ( $\bar{u} < 0$ ), that extends approximately one diameter downstream of the body (Fig. 3.4a & 3.5a). After the recirculation zone,  $\bar{u}$  increases rapidly back to  $U_\infty$ , following a  $-1/2$  power law (see fit shown in Fig. 3.4a & 3.5a). This is consistent with previous studies of plane wakes, for which the velocity deficit,  $U_\infty - \bar{u}_{y=0}$ , varies as  $x^{1/2}$  (Pope, 2000). The total length of the wake,  $L$ , is defined as the distance from the downstream end of the patch ( $x = D$ ) to a point where the rate of velocity recovery is reduced to  $\frac{\partial(\bar{u}/U_\infty)}{\partial(x/D)} < 0.1$ . For the solid bodies of  $D = 22\text{cm}$  and  $42\text{cm}$  shown in Figure 3.4a and 3.5a,  $L = 65\text{cm}$  and  $140\text{cm}$ , respectively. The dimensionless wake length is  $L/D = 3.0$  and  $3.3$ , and the Reynolds number is  $Re_D = U_\infty D/\nu = 2.2 \times 10^4$  and  $4.1 \times 10^4$ , accordingly. These values are consistent with previous studies. Cantwell and Coles (1983) reported  $L/D = 2.5$  for a cylinder wake at  $Re_D = 1.4 \times 10^5$ . Kravchenko and Moin (1999) numerically studied the flow past a circular cylinder at  $Re_D = 3900$ , and they found  $L/D = 3$ .

The wakes behind the porous patches are distinct from those behind the solid body. To start, consider the porous patch of  $\Phi = 0.03$  and  $D = 22\text{cm}$  shown in Figure 3.4c. Downstream of the patch the velocity continues to decrease, and a diverging flow ( $\bar{v} > 0$ ) is observed until roughly  $x = 60\text{ cm}$  ( $x/D \approx 3$ , or  $2D$  beyond the end of the patch). Beyond this point,  $\bar{u}$  is constant until  $x = 200\text{cm}$  (Fig. 3.4c). This region of uniform velocity is called the steady wake, and the uniform velocity is denoted as  $U_1$ . For the patch of  $\Phi = 0.03$  and  $D = 22\text{cm}$ ,  $U_1 = 5.8\text{ cm/s}$  (Fig. 3.4c). In this case, the steady wake extends from the end of the patch ( $x = D = 22\text{cm}$ ) to  $x = 200\text{cm}$ , a distance denoted as  $L_1$ . For this case (Fig. 3.4c),  $L_1 = 200\text{cm} - 22\text{cm} = 178\text{cm}$  ( $L_1/D = 8.1$ ). The magnitudes of  $U_1$  and  $L_1$  for each case are given in Table 3.1. In general, both  $U_1$  and  $L_1$  decrease as  $\Phi$  increases, and  $L_1 = 0$  for  $\Phi = 1$  (solid body). For the same  $\Phi$ ,  $L_1$  decreases as  $D$  decreases, but  $U_1$  is not a function of  $D$ . These trends are discussed in greater detail later.

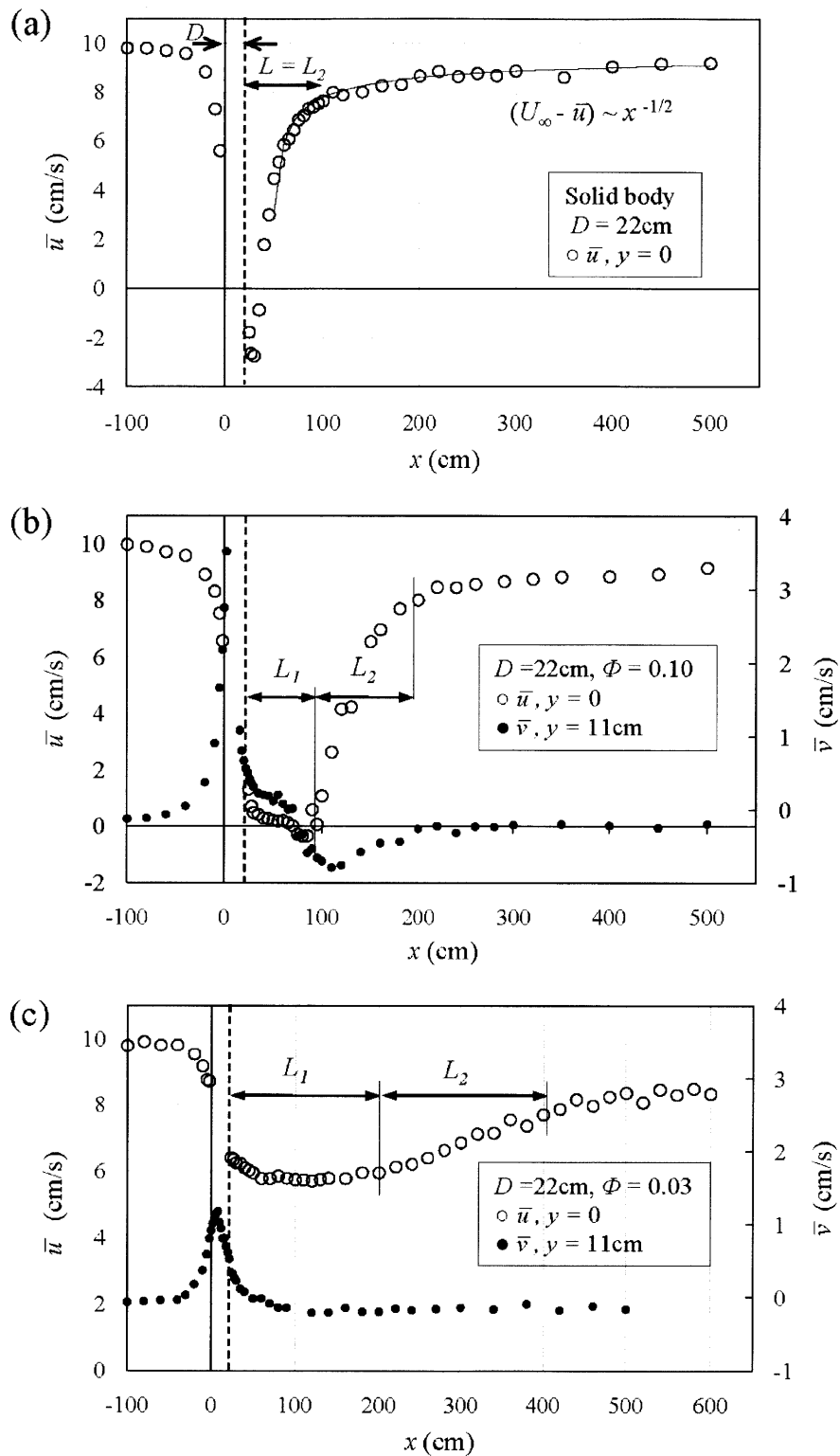


Figure 3.4 Longitudinal velocity profiles for patches with  $D = 22\text{cm}$ . (a) solid body, (b)  $\Phi = 0.10$ , (c)  $\Phi = 0.03$ . Patch is from  $0 < x < D$ . The dashed line indicates the downstream end of the patch. Note that the longitudinal velocity is given on the left hand axis, and the lateral velocity is given on the right hand axis.

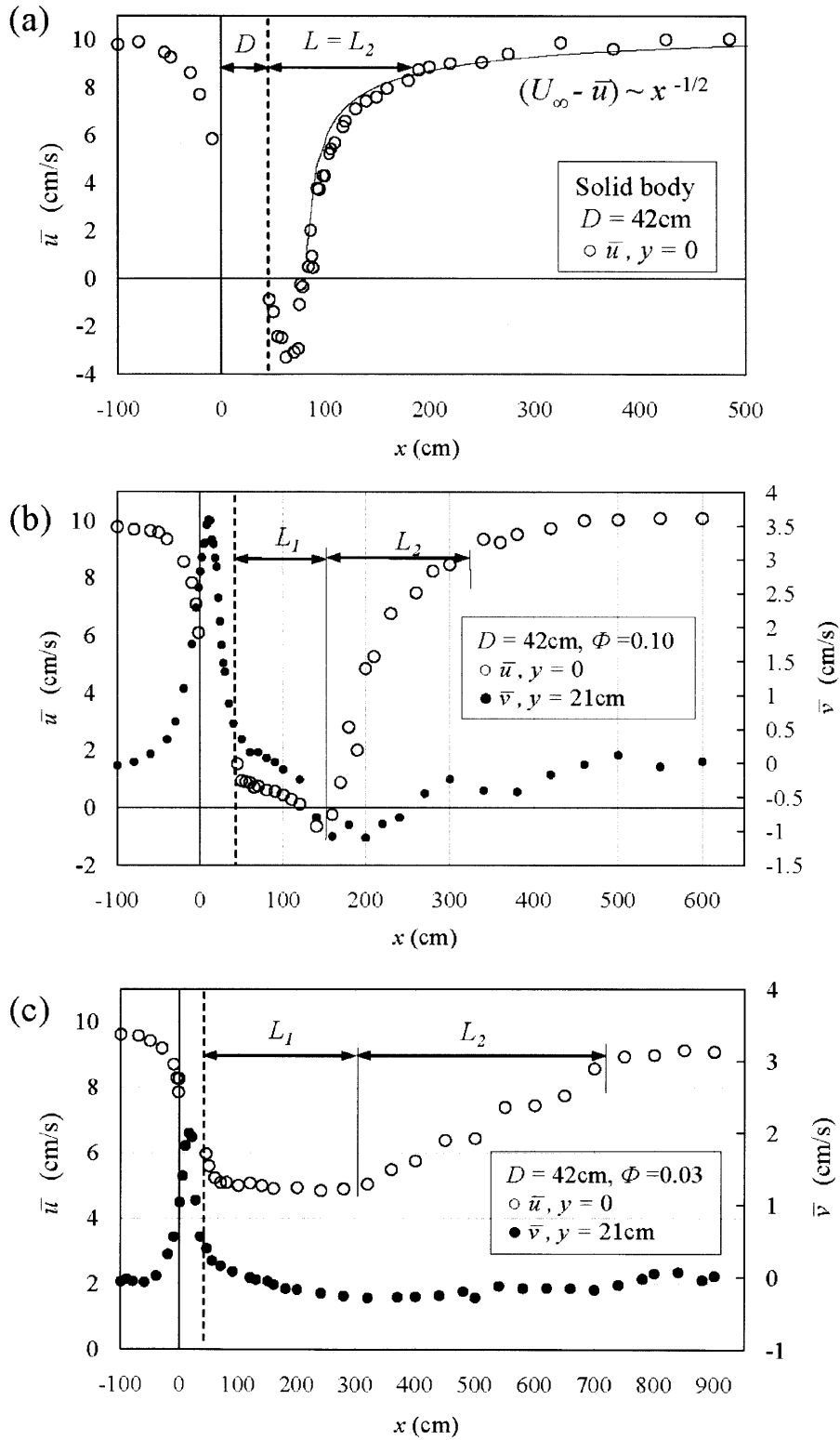


Figure 3.5 Longitudinal velocity profiles of patches with  $D = 42$  cm. (a) solid body, (b)  $\Phi = 0.10$ , (c)  $\Phi = 0.03$ . Patch is from  $0 < x < D$ . The dashed line indicates the downstream end of the patch.

As the patch becomes denser ( $\Phi$  increases) and  $U_1$  decreases, the diversion of flow increases ( $\bar{v}$  increases). Please note that  $\bar{v}$  is given on right-hand axis in Figure 3.4 and 3.5. For  $D = 22\text{cm}$ , maximum  $\bar{v}$  increases from 1.2 cm/s to 3.5 cm/s as  $\Phi$  increases from 0.03 to 0.10 (Fig. 3.4b & c). Similarly, for the cases with  $D = 42\text{cm}$  (Fig. 3.5b & c), maximum  $\bar{v}$  increases from 2.0 cm/s to 3.6 cm/s with  $\Phi$  increasing from 0.03 to 0.10.

After the steady wake region ( $x > D + L_1$ ), the velocity increases, recovering toward the free stream velocity,  $U_\infty$ . The total length of the wake ( $L$ ) is defined the same way as for the solid body, given above. The wake recovery region has a length-scale  $L_2 = L - L_1$  (reported in Table 3.1). For example, in Figure 3.4c,  $L_2 = 200\text{ cm}$  ( $L_2/D = 9.1$ ), and the total longitudinal extent of the wake is  $L = L_1 + L_2 = 378\text{ cm}$  ( $L/D = 17.2$ ). For the solid body case, the region  $L_1$  is absent (*i.e.*  $L_1 = 0$ ,  $U_1 = 0$ ) and the length of the wake is  $L = L_2$ . For the solid body of  $D = 22\text{ cm}$ ,  $L = L_2 = 65$  ( $L/D = 3.0$ ), which is significantly shorter than the wake of the porous patch of the same size with  $\Phi = 0.03$  (Fig. 3.4). The rate of velocity recovery can be compared using  $(U_\infty - U_1)/L_2$ . For  $D = 22\text{cm}$  (Fig. 3.4),  $(U_\infty - U_1)/L_2 = 0.15, 0.11, 0.02$  for  $\Phi = 1, 0.10$  and  $0.03$ , respectively. That is, the rate of velocity recovery declines with decreasing solid volume fraction,  $\Phi$ . Similarly, for  $D = 42\text{cm}$  (Fig. 3.5),  $(U_\infty - U_1)/L_2 = 0.07, 0.05, 0.01$  for  $\Phi = 1, 0.10$  and  $0.03$ , respectively. In the wake recovery region ( $L_2$ ), the transverse velocity is negative ( $\bar{v} < 0$ ), indicating a flux towards the center of the wake, which is consistent with the wake-scale flux of momentum achieved by the large-scale vortices (Fig. 3.4 and 3.5). After  $L_2$ ,  $\bar{v}$  remains small because the velocity deficit in the wake is close to zero.

A flow reversal, indicative of a recirculation zone, is present in the wakes behind the dense patches ( $\Phi = 0.10$  in Fig. 3.4b and 3.5b), but is absent in the wakes of the sparser patches ( $\Phi = 0.03$  in Fig. 3.4c and 3.5c). Specifically,  $\bar{u} < 0$  between  $x = 70\text{ cm}$  and  $x = 80\text{ cm}$  for  $D = 22\text{ cm}$  (Fig. 3.4b) and between  $130\text{ cm}$  and  $160\text{ cm}$  for  $D = 42\text{ cm}$  (Fig. 3.5b). The length of the recirculation zone is a bit smaller for the porous patches than for the solid body, for which the recirculation extended over length-scale  $D$ , as discussed above. Castro (1971) observed a recirculation zone behind perforated plates with low porosity ( $\beta = 0$  to  $0.305$ ). For the solid plate ( $\beta = 0$ ), the recirculation zone was attached to the plate. As the porosity increased, the recirculation zone moved downstream. For the highest porosity considered by Castro ( $\beta = 0.425$ ), no recirculation zone was observed.

Next, consider the lateral wake structure and its evolution downstream. The lateral profiles of  $\bar{u}$  and  $v_{rms}$  for the solid patch of  $D = 22\text{ cm}$  are shown in Figure 3.6. One profile taken upstream of the body ( $x/D = -3.6$ ) is included for reference. Behind the solid patch, the velocity deficit,  $(U_\infty - \bar{u}_{y=0})$ , decreases as  $x$  increases. The transverse velocity fluctuation,  $v_{rms}$ , is maximum at the center of the wake, and decreases monotonically toward the edge of the wake, which is a signature of a vortex street (Townsend 1947; Lyn

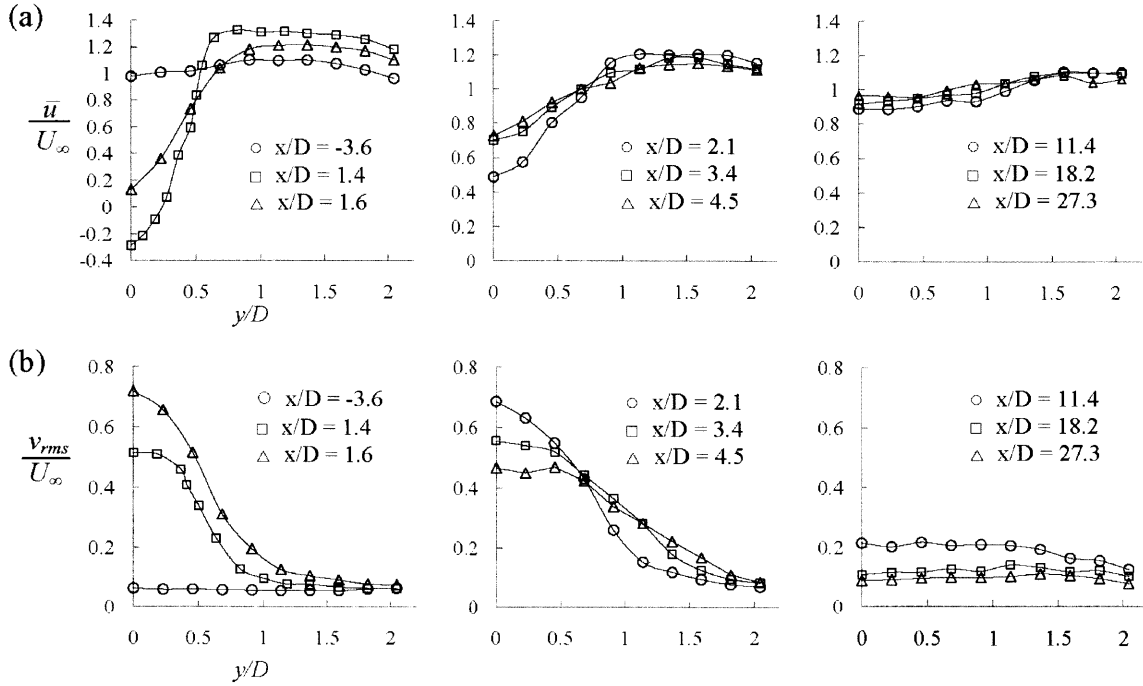


Figure 3.6 Lateral profiles of (a)  $\bar{u}/U_\infty$  and (b)  $v_{rms}/U_\infty$  for the solid circular body of  $D = 22\text{cm}$ . Due to the symmetry about the centerline ( $y/D = 0$ ), measurements were only made on one side of the flume ( $0 < y/D < 2$ ). The solid body is from  $-0.5 < y/D < 0.5$  and  $0 < x/D < 1$ .

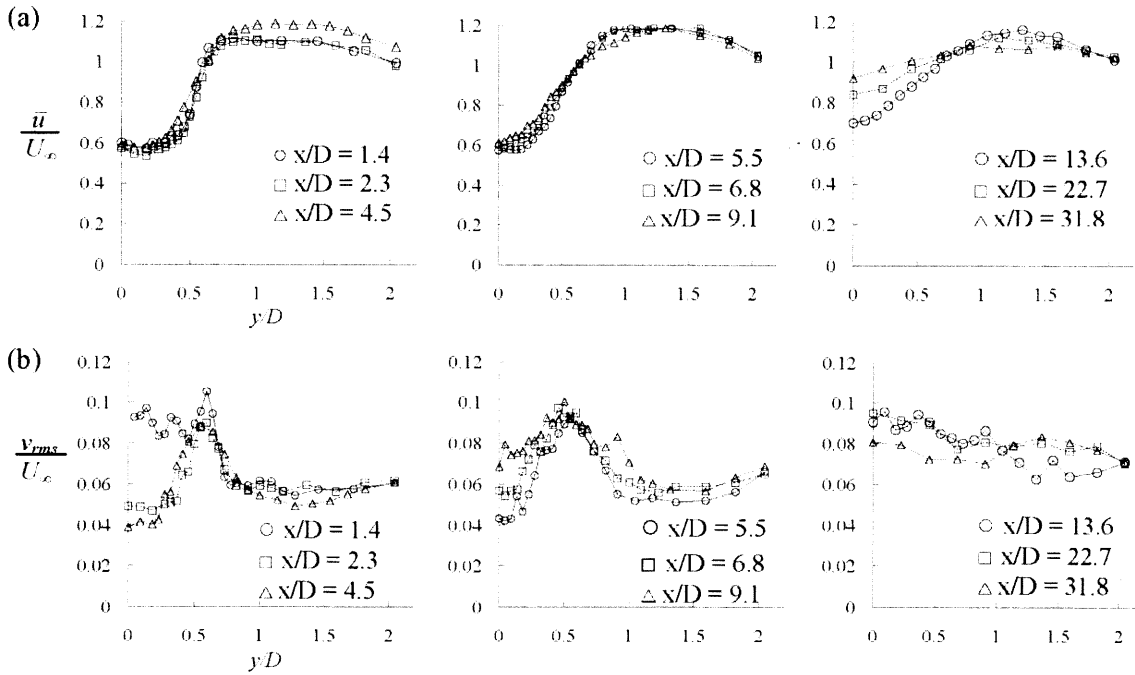


Figure 3.7 Lateral profiles of (a)  $\bar{u}/U_\infty$  and (b)  $v_{rms}/U_\infty$  for the patch of  $D = 22\text{cm}$ ,  $\Phi = 0.03$ .

et al. 1995). The maximum value of  $v_{rms}$  at centerline ( $y/D = 0$ ) decreases with distance downstream, due to the decay of the wake-scale turbulence.

In contrast to the solid body wake, behind the porous patch there is a steady wake region ( $L_I$ ) within which the velocity deficit at the centerline does not change with longitudinal distance (see profiles for  $x/D < 9.1$  in Fig. 3.7a). Very close to the patch,  $x/D = 1.4$ , the mean velocity across the wake is laterally uniform and lower than the velocity outside the wake ( $y/D > 0.7$ ). At this same position, the turbulence ( $v_{rms}$ ) in the middle of the wake ( $y/D < 0.5$ ) is higher than the level outside the wake (Fig. 3.7b). This region of elevated turbulence directly behind the patch is due to the small-scale turbulence generated by individual cylinders. This cylinder-scale turbulence dissipates quickly, disappearing before the next profile at  $x/D = 2.3$  (Fig. 3.7b). At  $x/D = 2.3$ , the narrow peak of  $v_{rms}$  at the edge of the wake ( $y/D \approx 0.5$ ) is associated with the shear-layer developing between the diminished velocity within the wake and the higher velocity of the free stream. A similar shear layer is present on the opposite side of the wake (not shown). Close to the patch, the two regions of high shear at the wake's outer edges are separated by the central region of uniform flow (similar to a bleed flow), and the shear layers develop individually with distance from the patch. The profiles from  $x/D = 1.4$  to  $x/D = 9.1$  (*i.e.* the steady wake region) show a constant velocity at the center of the wake ( $U_I$ ), and the velocity gradient at the edge of the wake decreases as the shear layer grows. The growth of the shear layer can also be seen in the profiles of  $v_{rms}$ , as the peak of  $v_{rms}$  becomes wider, until eventually at  $x/D = 9.1$  the shear-layers merge at the centerline (Fig. 3.7b). Beyond  $x/D = 9.1$ , the shear layers begin to interact to form the von Karman vortex street, and  $\bar{u}$  at the centerline starts to increase, due mostly to the enhanced transverse mixing associated with the wake-scale vortices. At  $x/D = 13.6$ ,  $v_{rms}$  is maximum in the middle of the wake, corresponding to a single street of large vortices. Note that the peak  $v_{rms}$  is lower for the porous patch (Fig. 3.7) than for the solid body (Fig. 3.6), indicating weaker wake-scale oscillations behind the porous patch. The appearance of the vortices at  $x = D + L_I$  is confirmed by flow visualization, which is discussed below.

In the wake behind a solid body there is a single peak in  $v_{rms}$  at the centerline ( $x/D = 2$  in Fig. 3.8a), associated with the formation of the von-Karman vortex street (Bearman 1965; Lyn et al. 1995). In contrast, two distinct zones of elevated turbulence can be identified in the wake behind the porous patch. First, there is a small peak of  $v_{rms}$  directly behind the patch ( $x/D = 1$ , Fig. 3.8), associated with the small-scale turbulence generated in the wake of individual cylinders. These small eddies die out quickly. A second maximum in  $v_{rms}$  appears at the formation of the patch-scale vortices. For  $\Phi = 0.10$  in Figure 3.8a and b, the peak at  $x/D = 5$  is nearly as distinct as that behind the solid body. As  $\Phi$  decreases (compare  $\Phi = 0.10$  and  $0.03$  in Fig. 3.8), the second peak in  $v_{rms}$  becomes lower, spans a longer longitudinal distance, and moves further downstream. The position and magnitude of  $v_{rms,max}$  are reported in Table 3.1. Note that

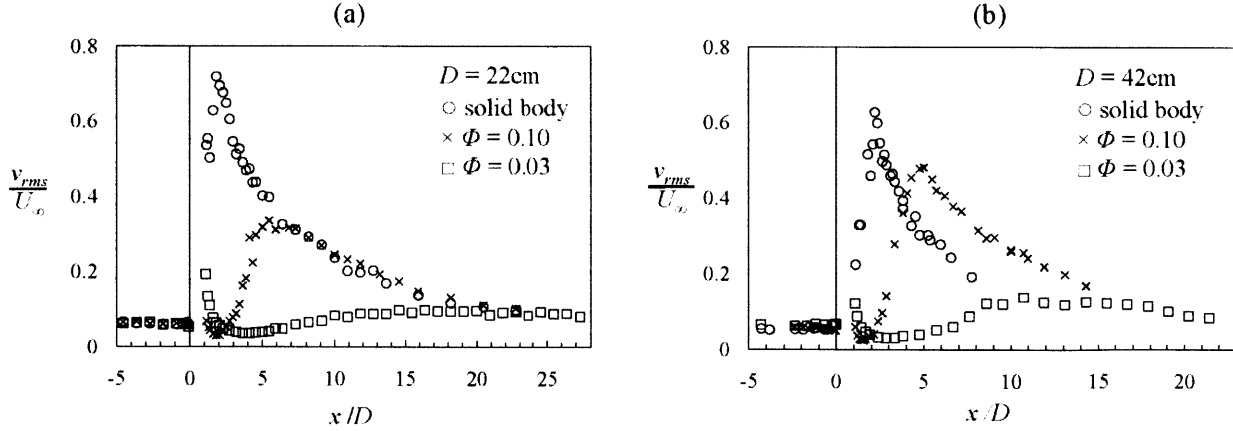


Figure 3.8 Longitudinal profile of  $v_{rms}/U_\infty$  at the centerline,  $y=0$ ; (a)  $D = 22\text{cm}$ , (b)  $D = 42\text{cm}$ . Patch is from  $0 < x/D < 1$ .

the position of  $v_{rms,max}$  is measured from the downstream end of the patch. Since the vortex is formed from the interaction of two shear-layers, the position of  $v_{rms,max}$  is always downstream of the steady wake region  $L_1$ , consistent with the observation by Wood (1967). Because the turbulence intensity ( $v_{rms,max}$ ) weakens as  $\Phi$  decreases, velocity recovery is slower, *i.e.*  $L_2/D$  increases as  $\Phi$  decreases (Table 3.1).

The two distinct scales of turbulence present in the wake of the porous patch can be seen in the velocity spectra (Fig. 3.9). First consider the patch of  $D = 22\text{cm}$  and  $\Phi = 0.03$ . At a location close to the downstream end of the patch ( $x = 24\text{ cm}$ ,  $x/D \approx 1$ , Fig. 3.9a), there is a narrow peak in  $S_{vv}$  at  $f_d = 2\text{ Hz}$ . This corresponds to turbulent energy at the scale of the individual cylinders. Specifically, the cylinder Reynolds number is  $Re_d = \frac{U(x = D, y = 0) \times d}{\nu} = 400$ , and its Strouhal number is

$$St_d = \frac{f_d d}{U(x = D, y = 0)} = 0.18. \text{ The frequency is consistent with the vortex shedding of a solid cylinder, } St$$

$\approx 0.2$  for  $200 < Re < 3 \times 10^5$  (Roshko 1961; Schewe 1983). Further downstream in the same wake ( $x = 300\text{ cm}$ ,  $x/D \approx 14$ , corresponding to the position of  $v_{rms,max}$ , Fig. 3.9b), the peak frequency in the spectrum shifts to  $0.1\text{ Hz}$ , which corresponds to the von-Karman vortex street. In fact, for all patches of diameter  $D = 22\text{ cm}$ , the velocity spectrum measures at the locations of the  $v_{rms,max}$  (Fig. 3.9b, d, e) contained the same dominant frequency,  $f_D = 0.1\text{ Hz}$ , which corresponds to the vortex shedding frequency of a solid cylinder of diameter  $D = 22\text{ cm}$ . Specifically,  $St_D = \frac{f_D D}{U_2} = 0.17$ . Note that  $U_2$  is used instead of  $U_\infty$ , as a more

representative value for the outer shear-layer velocity. By comparing the magnitude of the peaks in  $S_{vv}$  (Fig. 3.9b, d and e), note that the turbulence intensity of wake-scale vortices is greatest for the solid body (Fig. 3.9e,  $S_{vv} = O(10^4)$ ), and decreases with increasing patch porosity. Specifically, the peak is higher for

the dense porous patch (Fig. 3.9d,  $S_{vv} = O(10^3)$ ) than for the sparse patch (Fig. 3.9b,  $S_{vv} = O(10^2)$ ), which is consistent with the turbulence profiles shown in Fig. 3.8, *i.e.*  $v_{rms,max}$  is smaller for smaller  $\Phi$  (increasing porosity). For the case of  $D = 22\text{cm}$  and  $\Phi = 0.14$ , the velocity exiting the patch is too low to generate cylinder-scale turbulence,  $Re_d = O(10)$ , therefore there is no velocity fluctuation at the cylinder scale for this case, *i.e.* no peak in spectrum (Fig. 3.9c).

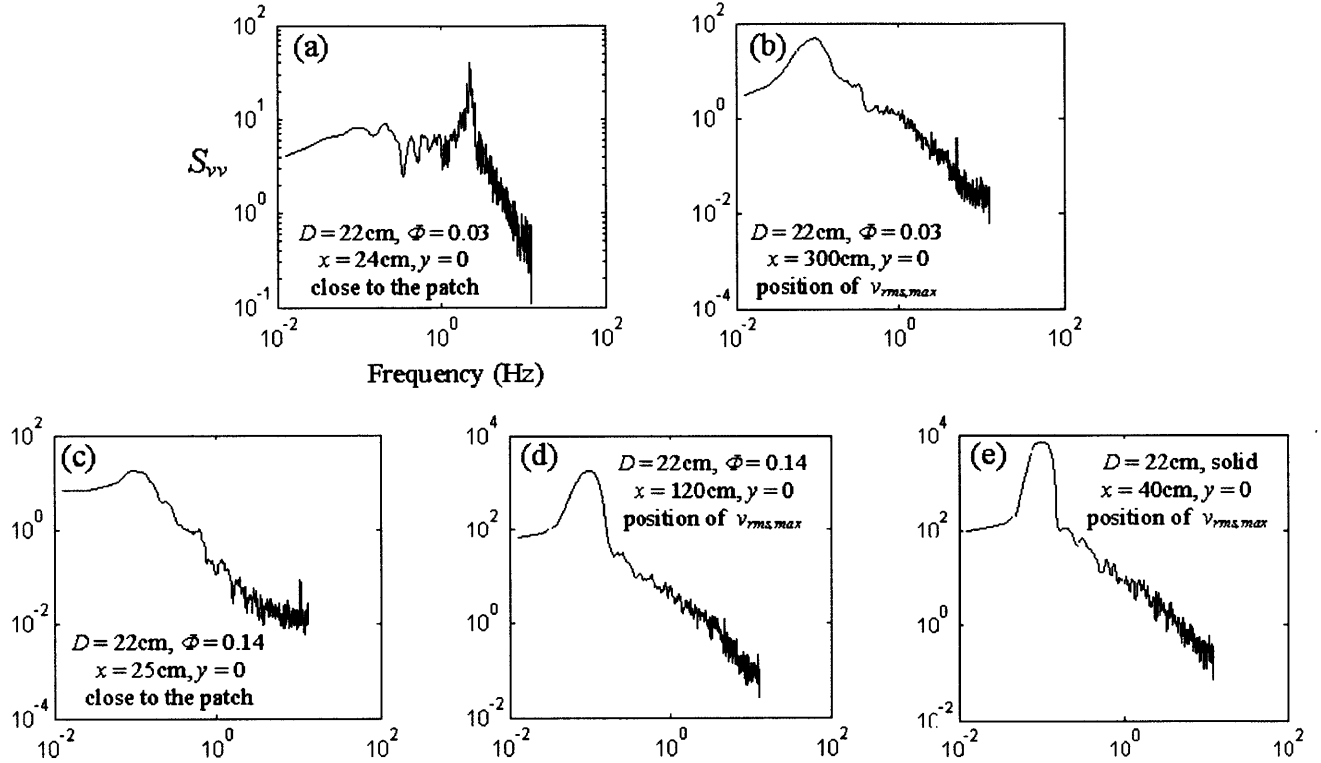


Figure 3.9 Power spectra measured on centerline directly behind the patch (a) and (c), and at the position of maximum  $v_{rms}$ , (b), (d), (e). (a) and (b) are for the patch of  $D = 22\text{cm}$ ,  $\Phi = 0.03$ ; (c) and (d) are for the patch of  $D = 22\text{cm}$ ,  $\Phi = 0.14$ ; (e) Solid body of  $D = 22\text{cm}$ .

After the two shear layers grow wide enough to interact and form a von-Karman vortex street, the velocity in the wake starts to increase back to the upstream velocity. The length of the velocity recovery region is called  $L_2$ . The recovery of the centerline velocity back to the free stream value is due to the cross-wake mixing driven by the wake-scale vortex street. The turbulence intensity is less for the porous body than for the solid body (Fig. 3.8) and consequently the length of the velocity recovery region ( $L_2$ ) is longer for the porous body wakes, compared to the solid body case (Fig. 3.10). Specifically,  $L_2/D$  increases with decreasing  $v_{rms,max}$ . The solid body cases (shown in solid markers) indicate that the lower limit of  $L_2/D$  is 3 (dashed line).

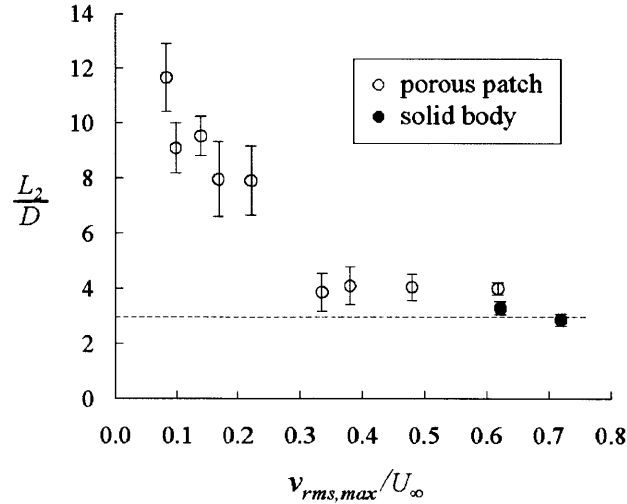


Figure 3.10 The relation between  $L_2/D$  and  $v_{rms,max}/U_\infty$ . The dashed line indicates the solid body limit.

### 3.3.2 Flow visualization

Flow visualization was used to observe both the steady wake region and the vortex street in the wake of a porous patch (Fig. 3.11). Images are grouped by patch size,  $D$ . For each patch size, the steady wake region becomes longer, and the lateral extent of the wake oscillation becomes smaller as  $\Phi$  decreases. The distance from the downstream end of the patch to the point where the two streaks of dye merge, denoted  $L_{1,dye}$ , is another measure of the steady wake region. For each case,  $L_{1,dye}$  was obtained by averaging the lengths measured from ten individual pictures (Table 3.1). The length-scales of the steady wake region measured from velocity profiles ( $L_1$ ) and from dye images ( $L_{1,dye}$ ) are the same within uncertainty (Fig. 3.12).

Pictures were taken every 2 seconds to examine the unsteadiness in the wake. The vortex frequency ( $f_D$ ) could be estimated from the series of pictures. The images also reveal that the vortices become increasingly irregular and intermittent as the solid volume fraction decreases. For example, in the case of  $D = 12\text{cm}$ ,  $\Phi = 0.04$  (Fig. 3.11c), the two dye streaks eventually mix downstream, but no clear pattern of oscillation occurs. Similarly in Castro's (1971) study of the wake behind a perforated plate, the vortex street ceases to form for the plates with porosity higher than 0.2. As the porosity increases, the velocity difference  $U_2 - U_1$  decreases, producing a smaller velocity gradient. When  $U_2 - U_1$  is too small, the instability is not strong enough to generate a vortex street, although weak oscillations are still identified in spectral analysis.

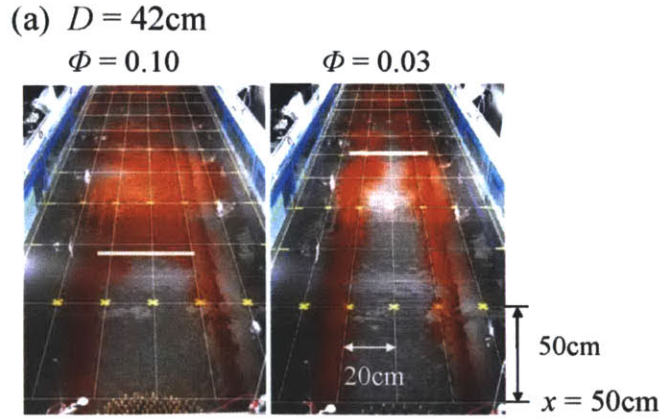
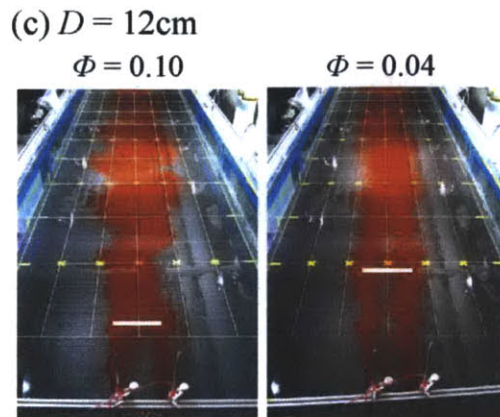
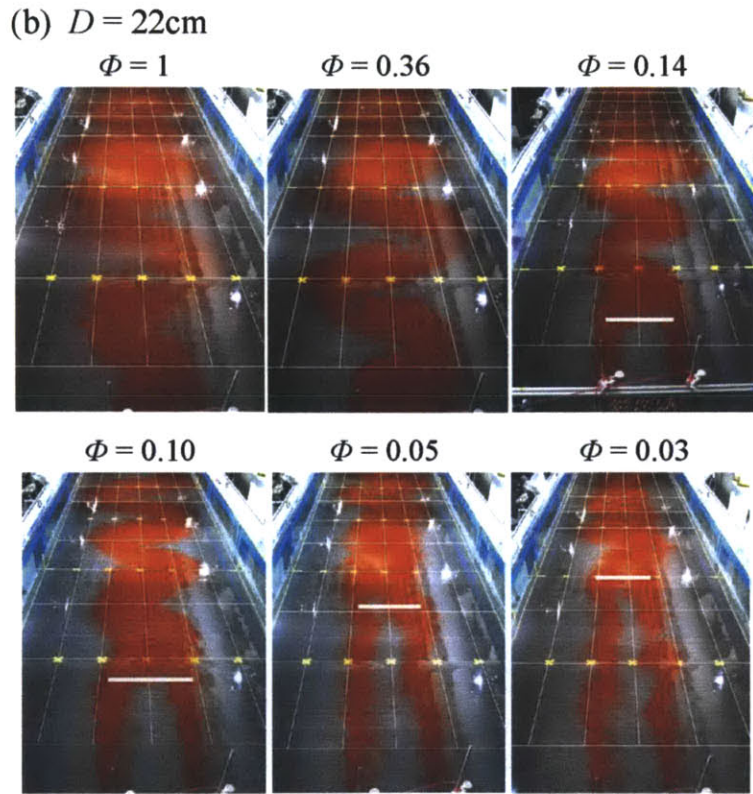


Figure 3.11 Flow visualization. The patch is at the bottom of the picture. Flow is from bottom to top. The dye was injected at the two outmost edges of the patch. The grids start from  $x = 50\text{cm}$  (from the leading edge of the patch) and mark the distance of  $50\text{cm}$  in  $x$ -direction and  $20\text{cm}$  in  $y$ -direction. The white bar indicates the end position of the steady wake ( $L_{1,dye}$ ). The values of  $L_{1,dye}$  are reported in Table 3.1. (a)  $D = 42\text{cm}$ ; (b)  $D = 12\text{cm}$ ; (c)  $D = 22\text{cm}$ .



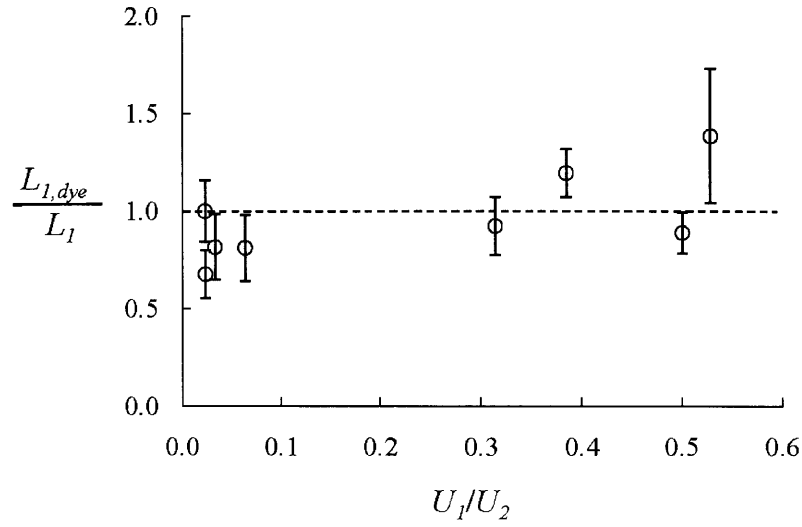


Figure 3.12 Comparison between  $L_1$  and  $L_{1,dye}$ .  $L_1$  is the length of the steady wake measured from longitudinal profile of  $\bar{u}$  at the centerline.  $L_{1,dye}$  is measured from the pictures of flow visualization.

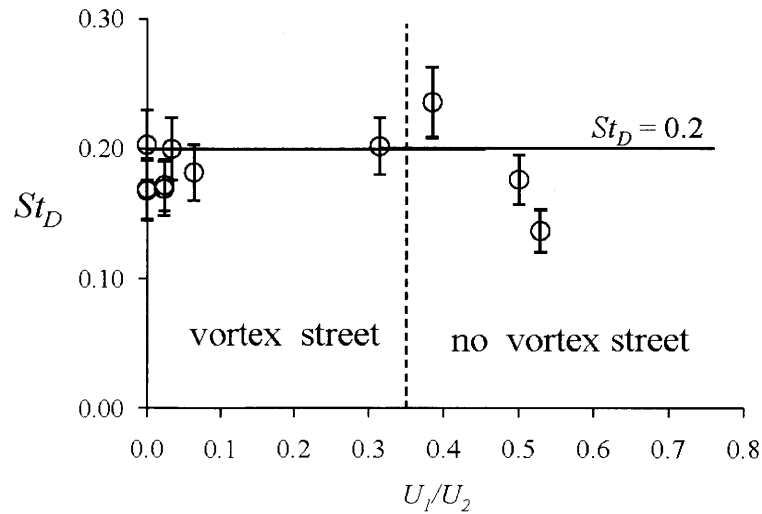


Figure 3.13 Strouhal number ( $St_D = f_D D/U_2$ ) versus the velocity ratio of  $U_1/U_2$ . Whether or not there is a vortex street is determined from the flow visualization. For the cases with the vortex street,  $f_D$  is obtained from the flow visualization. For the cases with no vortex street,  $f_D$  is obtained from  $S_{v_r}$ .

The Strouhal number,  $St_D = f_D D/U_2$ , based on the frequency obtained by flow visualization, is included in Table 3.1. Note that a distinct vortex street is not observed for  $\Phi \leq 0.035$ . The values of  $St_D$  estimated from the tracer images agree with the spectral peak estimates, also shown in Table 3.1. A distinct vortex street is observed for  $U_1/U_2 < 0.35$ , and no vortex street is observed for  $U_1/U_2 > 0.35$  (Fig. 3.13). Whether or not a vortex street was observed,  $St_D$  estimated from spectra was close to 0.2. For those cases without a visual vortex street, oscillation was still picked up in the spectra. For  $U_1/U_2 > 0.5$ ,  $St_D$  falls below 0.2. This suggests that as  $U_1/U_2$  increases,  $St_D$  decreases, which is intuitively correct, *i.e.* consider the limit of  $\Phi \rightarrow 0$  (no obstruction),  $U_1/U_2 \rightarrow 1$  and there is no instability,  $f_D \rightarrow 0$  and  $St_D \rightarrow 0$ .

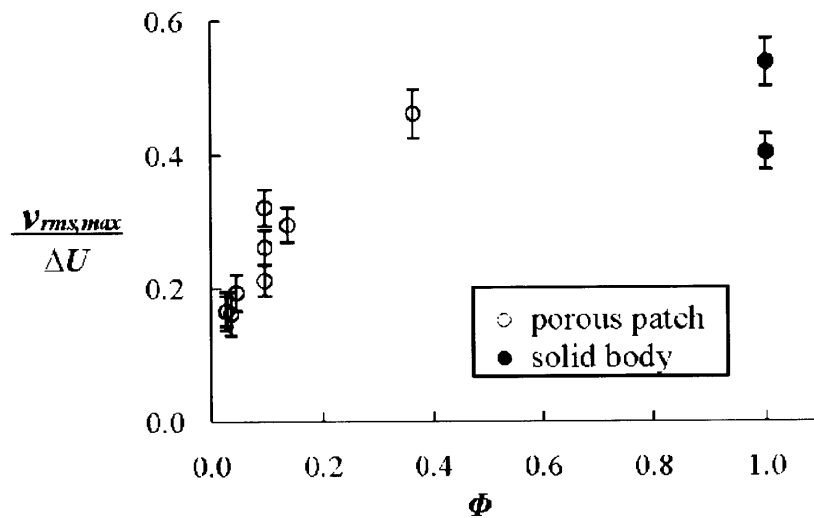


Figure 3.14 Turbulence intensity,  $v_{rms,max}$ , normalized by the velocity difference  $\Delta U = U_2 - U_1$

Finally, the porosity not only impacts the velocity difference  $\Delta U = U_2 - U_1$ , but also the efficiency with which this shear is converted to turbulence. Specifically, the ratio of  $v_{rms}/\Delta U$  decreases with decreasing  $\Phi$  (*i.e.* increasing porosity), as shown in Figure 3.14. This is consistent with changes in the vortex strength and coherence observed by flow visualization. Note that  $\Phi = 0.4$  is close to the solid body limit  $v_{rms,max}/\Delta U = 0.5$ . In addition, since  $v_{rms,max}$  is positively related with the velocity difference,  $\Delta U$  (Fig. 3.14), and the rate of the velocity recovery depends on the turbulence intensity of the wake oscillation (shown in Fig. 3.10),  $L_2$  increases with increasing  $U_1/U_2$ . Figure 3.15 shows this trend of  $L_2/D$  and  $L/D$  increasing with increasing  $U_1/U_2$ . The solid body cases correspond to  $U_1/U_2 = 0$  and  $L/D = L_2/D \approx 3$ .

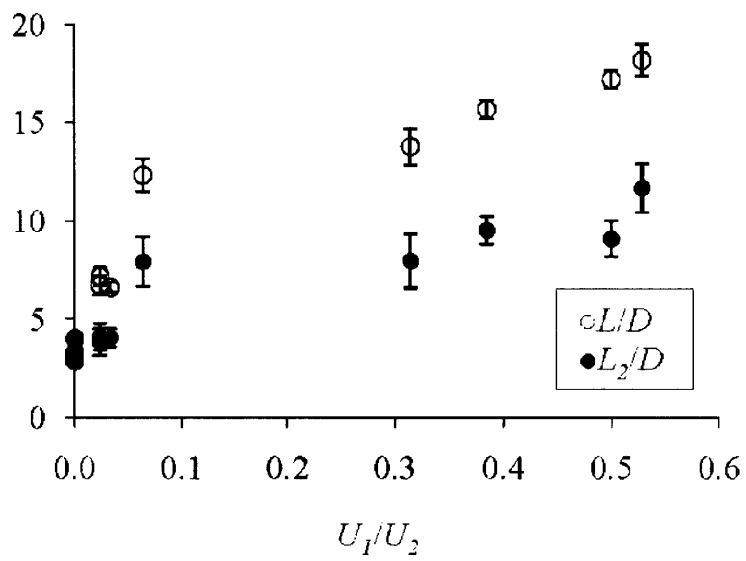


Figure 3.15  $L_2/D$  and  $L/D$  versus the velocity ratio of  $U_1/U_2$

### 3.4 Discussion

#### 3.4.1 Steady wake region and growth of the shear layer ( $L_1$ )

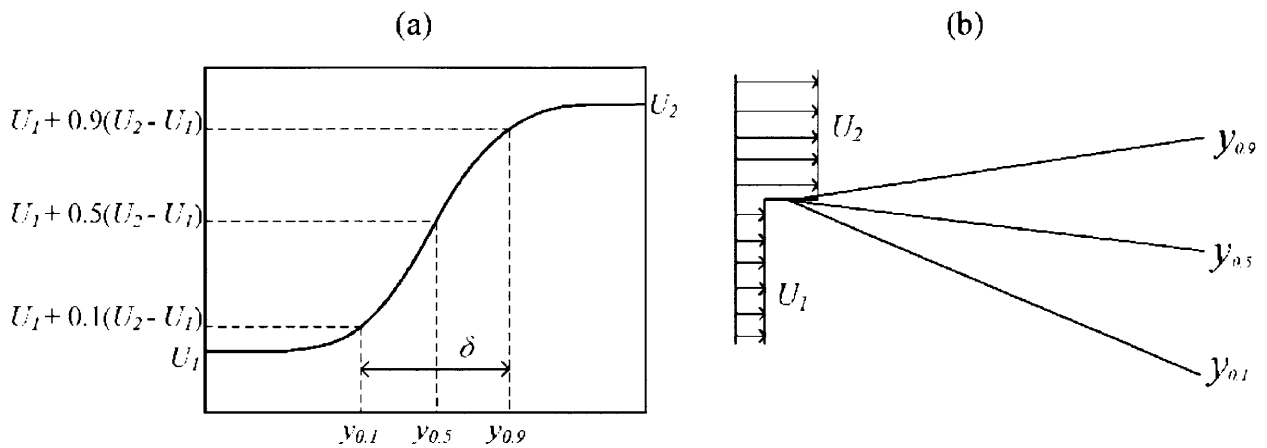


Figure 3.16 The plane shear layer. (a) Definition of shear layer width,  $\delta = y_{0.9} - y_{0.1}$ . (b) Axial variations of  $y_{0.1}$ ,  $y_{0.5}$  and  $y_{0.9}$ .

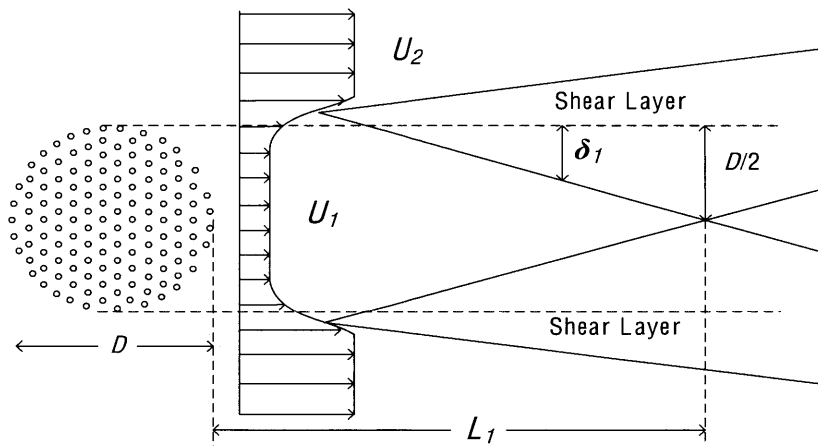


Figure 3.17 Schematic sketch of the shear layer growth in  $L_1$ , and the definition of  $\delta_1$ .

In the steady wake region behind the porous patch, shear layers at the two wake edges grow until they meet at the middle of the wake, after which a single vortex street can form. The length of the steady wake region,  $L_1$ , is therefore determined by the growth rate of the individual shear layers and the patch diameter, which sets the initial width of the wake. Drawing on previous descriptions of planar shear layer growth (*e.g.* Champagne et al. 1976), the characteristic width of the shear layer is  $\delta$  (Fig. 3.16a). Given the mean velocity within the shear layer,  $\bar{U}$ , and the velocity difference,  $\Delta U$ , the shear layer growth rate is

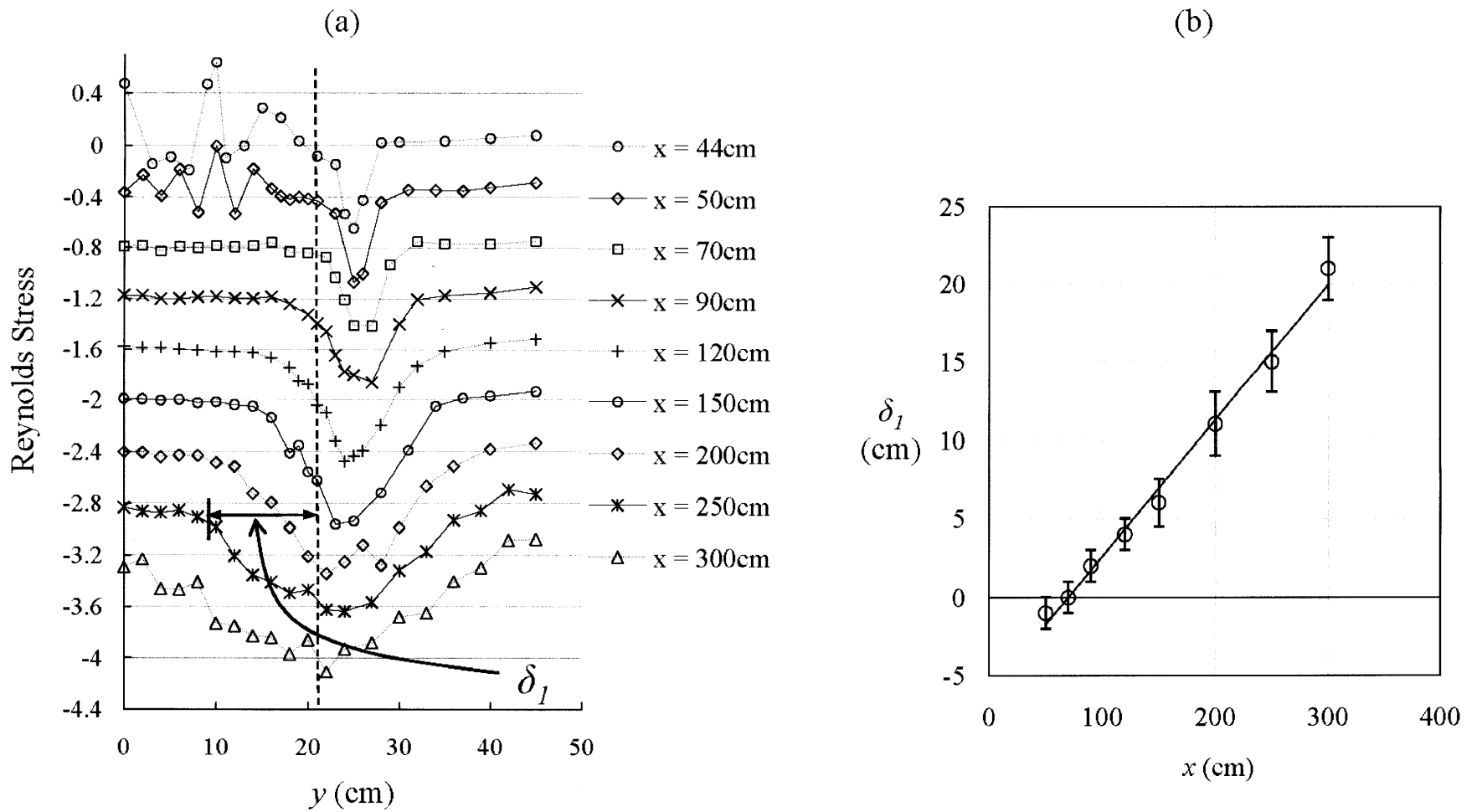


Figure 3.18  $D = 42$ cm and  $\Phi = 0.03$ . (a) The lateral profiles of Reynolds Stress. Profiles are offset by  $-0.4$  from previous profiles.  $\delta_1$  is measured from the edge of the patch (dash line,  $y = D/2 = 21$ cm) to the inner edge of the negative peak of the Reynolds Stress. (b) The width of the shear layer,  $\delta_1$ , as a function of  $x$ . The slope and its uncertainty is obtained by linear regression with 95% confidence level,  $d\delta_1/dx = 0.087 \pm 0.008$ .

$$\frac{d\delta}{dx} = S \frac{\Delta U}{\bar{U}} \quad (3.1)$$

$S$  is an empirical parameter which is constant over a wide range of  $\Delta U/\bar{U}$ . Dimotakis (1991) reports  $S \approx 0.06$  to  $S \approx 0.11$ . Champagne et al. (1976) found  $S \approx 0.097$ . The shear layer grows linearly and preferentially into the low velocity stream (Fig. 3.17b). The length-scale  $\delta$  is the distance between the positions of  $y_{0.9}$  and  $y_{0.1}$ . In this study I am only interested in how fast the shear layers grow toward the center of the wake, and at what  $x$  position they reach the centerline, so that I am only interested in the position of  $y_{0.1}$ . A new width,  $\delta_1$ , is defined as the distance from the edge of the patch,  $y = D/2$ , to  $y_{0.1}$  (Fig. 3.18). Using a formula similar to Eq. (3.1),  $S_1$  is the growth parameter for  $\delta_1$ . The low velocity within the steady wake is  $U_1$  and the velocity outside the wake is  $U_2$ , such that  $\bar{U} = (U_1 + U_2)/2$  and  $\Delta U = U_2 - U_1$ . Rearranging Eq. (3.1),  $S_1$  can be obtained from  $d\delta_1/dx$ ,

$$S_1 = (d\delta_1/dx) (\bar{U} / \Delta U). \quad (3.2)$$

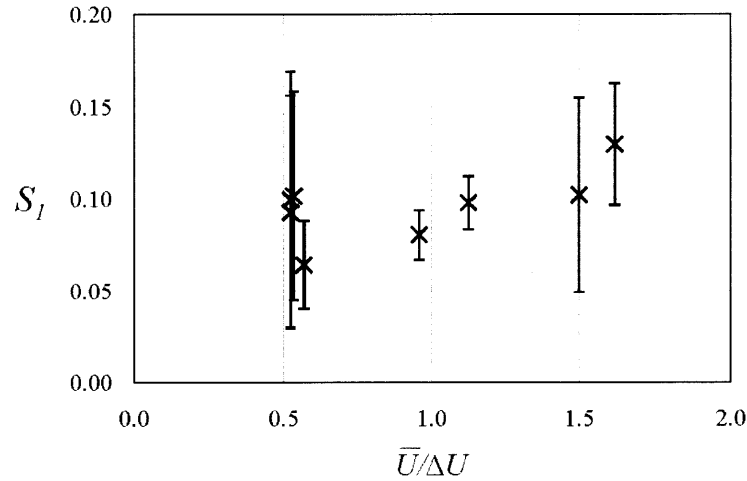


Figure 3.19 The values of  $S_1$  determined from Eq. (3.2) versus  $\bar{U}/\Delta U$ .

Lateral profiles of Reynolds stress ( $\overline{u'v'}$ ) within the region  $L_1$  were used to estimate  $d\delta_1/dx$ . For example, Figure 3.18a shows the lateral profiles of Reynolds stress for the patch of  $D = 42\text{cm}$ ,  $\Phi = 0.03$ . In each profile, the region of negative Reynolds stress corresponds to the shear layer. I define the inner edge of the shear layer as the point where the Reynolds stress reaches zero. Then,  $\delta_1$  is the distance from the inner edge of the shear layer to the edge of the patch ( $y = D/2$ , an example is shown in Fig. 3.18a).

The length-scale,  $\delta_1$ , measured for each profile shown in Figure 3.18a, is shown in Figure 3.18b, from which  $d\delta_1/dx = 0.089 \pm 0.008$ . Knowing  $U_1 = 5.0$  cm/s and  $U_2 = 13.0$  cm/s from Table 3.1,  $S_1 = 0.098 \pm 0.014$  is obtained from Eq. (3.2). The values of  $S_1$  obtained for all cases, and the corresponding values of  $\bar{U}/\Delta U$  are plotted in Figure 3.19. There is no clear trend between  $S_1$  and  $\bar{U}/\Delta U$ , so that I can assume  $S_1 = 0.10 \pm 0.02$  is a general constant. Using this value of  $S_1$ ,  $L_1$  can be estimated from the modified Eq. (3.2),  $d\delta_1/dx = S_1 \Delta U / \bar{U}$ . The length-scale  $L_1$  extends from  $x = D$  to a point where  $\delta_1 = D/2$ , therefore assuming  $\delta_1 = 0$  at  $x = D$ ,  $d\delta_1/dx = (D/2)/L_1$ , so  $L_1$  can be written as,

$$L_1 \approx \frac{D/2}{S_1} \frac{\bar{U}}{\Delta U} \quad (3.3)$$

The values of  $L_1$  predicted from Eq. (3.3) agree with the measured values within uncertainty (Fig. 3.20)

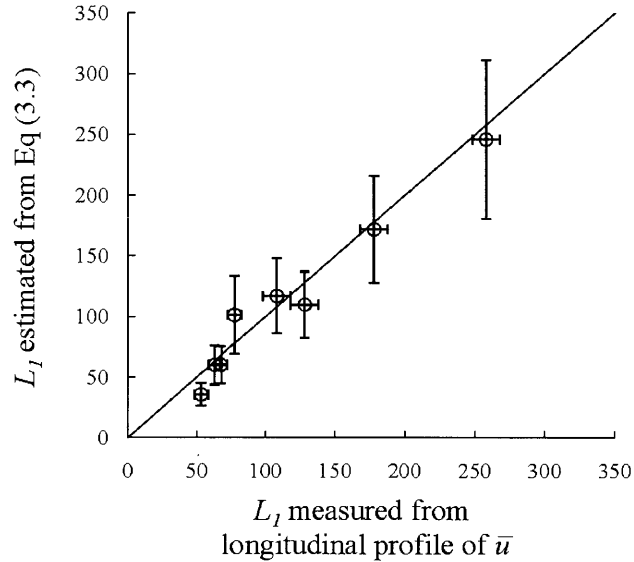


Figure 3.20 Comparison between  $L_1$  measured from longitudinal profiles of  $\bar{u}$  and  $L_1$  calculated from Eq. (3.3)

Wood (1967) and Ball et al. (1996) also studied the steady wake region using flow visualization. In Wood's experiment, particles were introduced in the channel flow but not into the base bleed flow. A clear region with no particles was observed directly behind the body. It indicated that the bleed flow did not mix with the outside flow for some distance behind the trailing edge,  $L_{Wood}$ , which has similar meaning as our  $L_1$ . Wood (1967) found that  $L_{Wood}$  increased as the velocity ratio of  $U_1/U_2$  increased ( $U_1$  is the bleed flow rate and  $U_2$  is the velocity outside the wake). Ball et al. (1996) injected dye at the center of the

upstream face of the square patch and the dye streak remained straight until some distance behind the patch,  $L_{Ball}$ , and then started to oscillate laterally. In our study, dye was injected at two sides of the circular patch. Similar to Wood's cases, a clear region behind the porous patch is observed and its length is denoted as  $L_{1,dye}$  (Table 3.1). The several observations of  $L_1$  ( $L_{Wood}$ ,  $L_{Ball}$ ,  $L_{1,dye}$ ,  $L_1$ ) are compared to the prediction of  $L_1$  (from Eq. 3.3) in Figure 3.21. A data point at  $L_1/D = 0$  and  $U_1/U_2 = 0$  represents the bluff body case which has no region  $L_1$ . All three studies show the same trend: dimensionless length,  $L_1/D$ , increases as  $U_1/U_2$  increases.  $L_{Ball}$  is close to our data.  $L_{Wood}$  has the same slope but is offset from the other studies by about  $D$ . The possible reason is that Wood's model is more streamlined, and in particular has a greater aspect ratio (length to width), so that the flow directly at the trailing edge is a parallel shear layer. However, in Ball's study and in the current study, the patch has an aspect ratio of 1, so that the flow at the trailing edge is not fully parallel, and additional flow diversion is observed after the body, which extends about one diameter long from  $x = D$ . Thus, for obstructions of aspect ratio 1, a parallel flow shear layer may not be achieved until one diameter downstream of the trailing edge, and this lengthens the steady wake by one diameter, consistent with the shift between Wood's measurements and the other studies (Fig. 3.21).

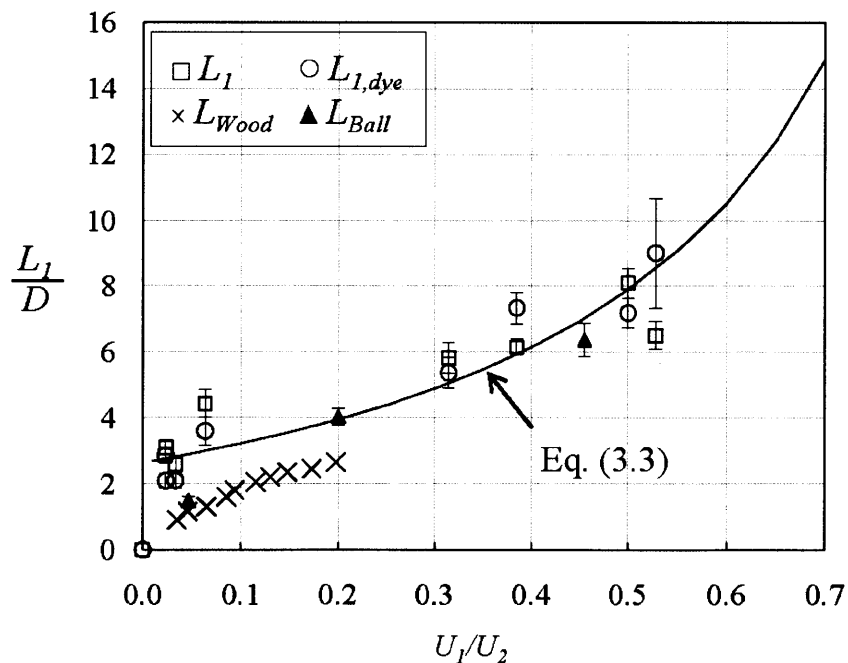


Figure 3.21 The relation between the dimensionless length of the steady wake,  $L_1/D$ , and the velocity ratio of  $U_1/U_2$ . The estimated value of  $L_1$  from Eq. (3.3) is represented in a solid line.

### 3.4.3 Magnitude of flow in the steady wake region ( $U_1$ )

The reduction in velocity from  $U_\infty$  to  $U_1$  depends on the drag imposed by the patch, which is related to both the size of the patch ( $D$ ) and its solid volume fraction ( $\Phi$ ). However, in the cases considered here,  $U_1$  depends only on  $\Phi$ , and is independent of  $D$  (Fig. 3.22). The square patches tested by Ball et al. (1996) are also included in Figure 3.22. For the patch  $\Phi = 0.36$ ,  $U_1/U_\infty$  is essentially zero, within measurement uncertainty, suggesting that the solid body limit is reached at around this value  $\Phi$ .

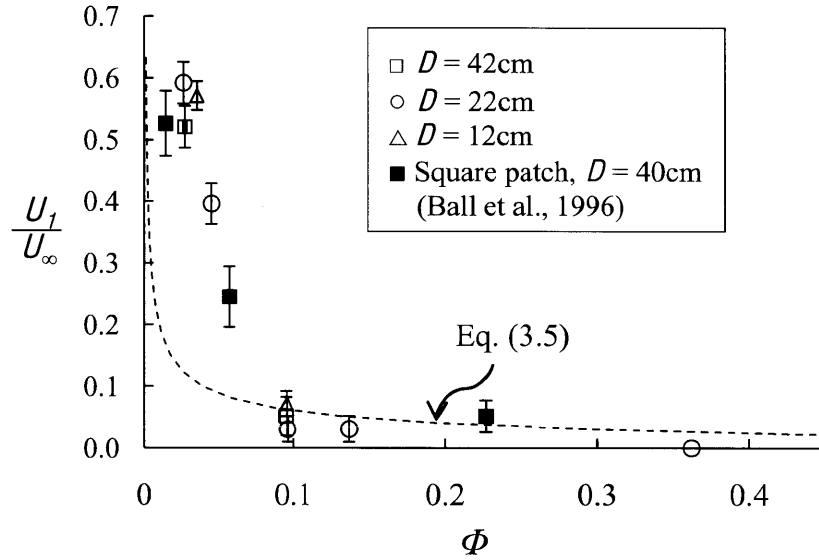


Figure 3.22 Velocity in the steady wake region ( $U_1$ ) as a function of the cylinder density ( $\Phi$ ). The estimation from Eq. (3.5) is represented in a solid line.

The lack of dependence on  $D$  can be explained by considering the results from Rominger and Nepf (2011), who describe the velocity deceleration through a long patch (length is much larger than the width). The velocity at the centerline starts to decline from some distance upstream of the patch, and the deceleration continues into the patch over a length  $x_D$ , after which flow reaches a steady velocity,  $U_o$ . Rominger and Nepf (2011) found that both the interior adjustment length ( $x_D$ ) and the final interior velocity ( $U_o$ ) depend on the dimensionless parameter,  $C_D a D$ , called the patch flow-blockage.  $C_D$  is the drag coefficient for the cylinders within the patch. In Rominger and Nepf (2011)  $D$  is the width of the rectangular patch. The scaling of  $x_D$  on  $C_D a D$  is

$$x_D \sim \frac{1}{C_D a} [1 + (C_D a D)^2] \quad (3.4)$$

For low flow-blockage ( $C_D a D < 1$ ),  $x_D$  is scaled with  $(C_D a)^{-1}$ . For high flow-blockage ( $C_D a D > 1$ ),  $x_D$  is scaled with  $D$  only. Using  $C_D = 1$  for simplicity, the estimated values of  $C_D a D$  for the patches tested in this study range from 0.8 to 17, *i.e.* nearly all cases fall clearly in the regime of high flow-blockage and therefore  $x_D$  scales on  $D$  only. If the patches were infinitely long, the flow would adjust to its interior velocity over the length-scale  $D$ . The circular patches studied here provide just this length, so  $U_I$  is expected to be equal to the interior velocity predicted for an infinite patch ( $U_I = U_0$ ). Rominger and Nepf (2011) show that, for high flow-blockage conditions,  $U_0$  is a function only of the solid volume fraction, consistent with our observations ( $U_I = f(\Phi)$ , Fig. 3.22). Specifically,

$$\frac{U_0}{U_\infty} = \sqrt{\frac{C_f}{h} \frac{(1-\Phi)}{C_D a}} = \sqrt{\frac{C_f}{C_D} \frac{d}{h} \left( \frac{1}{\Phi} - \Phi \right)} \quad (3.5)$$

The velocity predicted from Eq. (3.5), using the previously measured  $C_f = 0.006$ , the drag coefficient,  $C_D = 1$ , size of the cylinder,  $d = 0.6$  cm, and the water depth,  $h = 13.3$  cm, is shown with a dashed line in Figure 3.22. The agreement with the experimental results is excellent for  $\Phi \geq 0.1$ , for which  $C_D a D \geq 2$ , consistent with definition of high flow-blockage. For the sparse patches,  $\Phi \leq 0.05$ , the agreement between measured values and Eq. (3.5) degrades as the lower limit,  $C_D a D \approx 1$ , is approached.

If the patches were in the low flow-blockage regime ( $C_D a D < 1$ ), then the interior adjustment length would scale with  $(C_D a)^{-1}$ , which would be longer than  $D$ . In that case,  $U_I$  would be higher than the interior velocity predicted by Eq. (3.5), and I would expect  $U_I$  to be a function of both  $D$  and solid volume fraction. Indeed, at the lowest patch densities considered here ( $\Phi = 0.026, 0.035$ ,  $C_D a D = 0.8$  to 1.3) the measured velocity is higher than the prediction from Eq. (3.5).

### 3.5 Conclusion and areas of future research

The wake behind a porous body has two unique features compared to the wake behind a solid body. First, a steady wake region extends a distance  $L_I$  behind the body. Second, the formation of the von-Karman vortex street is delayed until the end of  $L_I$ . The flow exiting the patch is laterally uniform and slower than the flow that passes around the patch. In the steady wake region, stream-wise velocity at the centerline ( $U_I$ ) remains uniformly low relative to the upstream velocity and no transverse flow or lateral mixing occur. For the patch diameters and porosities considered here,  $U_I$  is a function of the porosity only. Close behind the patch, the wake contains small-scale turbulence generated in the wake of individual cylinders. Shear layers form at both sides of the wake. Initially, the two shear layers do not interact, and grow independently with distance downstream from the patch. The shear layers grow to the centerline at  $x = D + L_I$ , which marks the end of the steady wake.  $L_I$  increases as the patch porosity

increases. The length of the steady wake region ( $L_1$ ) can be estimated using the equation of the plane shear layer growth.

After the steady wake ( $L_1$ ), the von-Karman vortex street is formed from the interaction between the shear layers. The turbulence structure in this region is on the scale of the patch and dominates the transverse mixing across the wake which results in the velocity recovery. The maximum turbulence intensity behind a patch ( $v_{rms,max}$ ) is lower than that behind a solid body, which leads to a slower velocity recovery. As solid volume fraction decreases, and  $U_1/U_2$  increases, the vortex street weakens, losing some coherence, and for  $\Phi < 0.04$ , no vortex street is formed and only weak oscillation exists in the wake. Both the length of steady wake region ( $L_1/D$ ) and velocity recovery region ( $L_2/D$ ) are proportional to the solid volume fraction of the patch.

The unique features of the wake behind a short patch of vegetation might have some influence on the patterns of deposition and erosion, which in turn would affect the spatial structure of the patch (e.g. shape, distribution of stem density). Based on the flow structure discussed in this chapter, there are two extensions of this work.

(1) Use the method of measuring deposition, which is described in Chapter 2, to measure the spatially patterns of deposition inside and behind the patch. Due to the presence of the steady wake region, deposition is expected to be higher behind the patch than in the open channel. For some combination of stem density and flow condition, both the mean flow rate and turbulence intensity inside the patch is higher than behind the patch, which cause that the deposition inside the patch is lower than behind the patch.

(2) For the limit of a solid obstruction ( $\Phi = 1$ ), scouring is expected to occur around the edges, due to the acceleration of flow associated with the flow divergence. For the limit of no patch ( $\Phi = 0$ ), no erosion will occur. It is interesting to find out a critical stem density, below which the scouring around the patch will be prevented, and to examine the spatial patterns of sediment erosion.

These suggested future studies will lead to a better understanding of the growth of aquatic vegetation and improve the effectiveness of planting vegetation in river restoration.



## Chapter 4

### Conclusion

This thesis described two studies related to finite patches of emergent, rigid vegetation in a channel. For both studies, experiments were conducted in the same flume, and model vegetation patch was constructed from an array of rigid circular cylinder in a staggered arrangement. Chapter 2 (the first study) described the flow structure and the spatial pattern of deposition within and around a patch of model vegetation located at the sidewall of a channel (*i.e.* a partially vegetated channel). Two patch densities and three channel flow rates were tested. Along the flow-parallel edge of the patch, a shear layer formed due to the velocity difference between the open region and the vegetated region. The coherent vortices formed via Kelvin-Helmholtz stability and penetrated a distance  $\delta_v$  into the patch. Therefore the patch width was segregated into two parts, the outer region penetrated by the coherent vortices, and the inner region within which the stream-wise velocity remains laterally uniform. The water renewal in the outer region is much faster than that in the inner region due to the presence of these energetic vortices. The coherent vortices also induce an edge wave, which travels through both inner and outer regions, and enhance the lateral mass transport.

Particles were introduced to the flow in order to observe the patterns of the net deposition within and around the patch. The rate of net deposition depends on the flow condition and particle concentration. There are two sources of particle flux to the patch: the advection of particles across the upstream leading edge and the lateral dispersion of particles from the adjacent open channel. The relative contribution of these two supplies determines the spatial pattern of net deposition in the patch, if there is no resuspension. Using experimental results, a simple model was developed to find the value of the lateral dispersion coefficient. And longitudinal length scale over which particles entering through the leading edge of the patch can travel and a lateral length scale over which particles delivered by edge wave and turbulent diffusion through the flow-parallel edge can travel were found. They can be used to determine the region where particles cannot be delivered and deposition is limited by particle-supply.

In Chapter 3 (the second study), a circular patch of vegetation, which was small compared to the width of the channel, was examined. Three patch diameters and a wide range of patch density were tested. Velocity measurements and flow visualization were conducted to study the turbulent wake behind the patch. Compared to the wake behind a solid obstruction, the wake behind a patch of vegetation (*i.e.* a porous obstruction) has a region where the streamwise velocity ( $U_1$ ) remains steady and no transverse mixing occurs. This region, called the steady wake, has length  $L_1$ . For the solid body case,  $L_1 = 0$  and  $U_1 = 0$ . As the patch density decreases (*i.e.* porosity increases), both  $U_1$  and  $L_1$  increases. The flow exiting the patch is laterally uniform and slower than the flow that passes around the patch. Two shear layers form, one at either side of the wake. Initially, the two shear layers do not interact because they are separated by a region of uniform velocity, and they independently grow wider with distance downstream from the patch. Once they meet at the centerline, they start to interact and form a single von-Karman vortex street. The meeting point of the two shear layers marks the end of the steady wake region. A simple equation, based on plane shear layer growth, can be used to estimate the length of the steady wake region ( $L_1$ ).

After the steady wake, the velocity in the wake starts to recover towards the upstream value, due to the large scale transverse mixing driven by the von-Karman vortex street. The maximum turbulence intensity behind a patch ( $V_{rms,max}$ ) is lower than that behind a solid body, which leads to a slower velocity recovery. As the patch density decreases (*i.e.* porosity increases),  $V_{rms,max}$  decreases, resulting in a longer velocity recovery. The frequencies of the vortices are close to the vortex shedding frequency of a solid body. As the patch density decreases (*i.e.* porosity increases), the velocity shear decreases and the vortex street weakens, losing some coherence. For the case with the solid volume fraction smaller than 0.04, no vortex street is formed and only weak oscillation exists in the wake, which has a frequency less than the vortex shedding frequency.

## Reference

- Abt, S., W. Clary, C. Thornton, 1994. Sediment deposition and entrapment in vegetated streambeds. *J. Irrigation Drainage Eng.*, 120:1098-1110.
- Ball, D. J., P.K. Stansby, N. Alliston, 1996. Modelling shallow water flow around pile groups. *Proc. Instn Civ. Engrs Wat., Marit. & Energy*, 118, Dec., 226-236.
- Bearman, P.W., 1965. Investigation of the flow behind a two-dimensional model with a blunt trailing edge and fitted with splitter plates. *J Fluid Mech.*, 21(2), 241-255.
- Bennett, S. J., T. Pirim, B. D. Barkdoll, 2002. Using simulated emergent vegetation to alter stream flow direction within a straight experimental channel. *Geomorphology*, Vol. 44, Issues 1-2, 115-126.
- Betchov, R., W. Criminale, 1967. *Stability of Parallel Flows*. New York: Academic press. 449.
- Brookshire, E., K. Dwire, 2003. Controls on patterns of coarse organic particle retention in headwater streams. *J.N. Am. Benth. Soc.*, 22, 17-34., 27(8), 1020-1045.
- Cantwell, B., D. Coles, 1983. An experimental study of entrainment and transport in the turbulent near wake of a circular cylinder. *J. Fluid Mech.*, 136, 321-374.
- Castro, I. P., 1971. Wake characteristics of two-dimensional perforated plates normal to an air-stream. *J. Fluid Mech.*, 46 (3), 599-609.
- Champagne, F. H., Y. H. Pao, I. J. Wygnanski, 1976. On the two-dimensional mixing region. *J. Fluid Mech.*, 74, 209-250.
- Chandler, M., P. Colarusso, R. Buchsbaum, 1996. A study of eelgrass beds in Boston Harbor and northern Massachusetts bays. Office of Res. And Devel., US EPA, Narragansett, RI.
- Chen, D., G.H. Jirka, 1994. Experimental study of plane turbulent wakes in a shallow water layer. *Fluid Dyn. Res.*, 16, 11-41.
- Ciraolo, G., G. Ferreri, G. LaLoggia, 2006. Flow resistance of *Posidonia Oceanica* in shallow water. *J. Hyd. Res.*, 44(2), 189-202.
- Cotton, J., G. Wharton, J. Bass, C. Heppell, R. Wotton, 2006. The effects of seasonal changes to in-stream vegetation cover on patterns of flow and accumulation of sediment. *Geomorph.*, 77, 320-334.
- De Waal, L. C., A. R. G. Large, P. M. Wade, 1998. *Rehabilitation of Rivers: Principles and Implementation*, John Wiley and Sons, New York.
- Dimotakis, P. E., 1991. Turbulent free shear layer mixing and combustion. In S.N.B. Murthy and E.T. Curran (Eds.), *High-Speed Flight Propulsion Systems*, pp. 265-340. Washington: AIAA.

- Fischer, H., J. List, C.R. Koh, J. Imberger, N. Brooks, 1979. *Mixing in Inland and Coastal Waters*. Academic Press.
- Fonseca, M., J. Zieman, G. Thayer, J. Fisher, 1983. The role of current velocity in structuring eelgrass meadows. *Estuar. Coast. Shelf Sci.*, 17, 367–380.
- Gacia, E., C. Duarte, 2001. Sediment retention by a Mediterranean *Posidonia oceanica* meadow: The balance between deposition and resuspension. *Est. Coast. Shelf. Sci.*, 52(4), 505-514.
- Gambi, M., A. Nowell, P. Jumars, 1990. Flume observations on flow dynamics in *Zostera marina* (eelgrass) beds. *Mar. Ecol. Prog. Ser.*, 61, 159-169.
- Gedan, K. B., M. L. Kirwan, E. Wolanski, E. B. Barbier, B. R. Silliman, 2011. The present and future role of coastal wetland vegetation in protecting shorelines: answering recent challenges to the paradigm. *Climatic Change*, 106(1), pp7-29.
- Ghisalberti, M., Nepf, H., 2004. The limited growth of vegetated shear layers. *Water Resour. Res.*, 40, W07502, doi:10.1029/2003WR002776.
- Ghisalberti, M., H. Nepf, 2005. Mass transfer in vegetated shear flows. *Environ. Fluid Mech.*, 5(6), 527–551, doi10.1007/s10652-005-0419-1.
- Hill, M. T., W. S. Platts, 1998. Ecosystem Restoration: A Case Study in the Owens River Gorge, California. *Fisheries*, Vol 23, Issue 11, 18 – 27.
- Hosokawa, Y., and T. Horie. 1992. Flow and particulate nutrient removal by wetlands with emergent macrophytes, 1271-1282. *In* R. Vollenweider, R. Marchetti and R. Viviani, [eds.]. *Marine coastal eutrophication: Science of the total environment*. Elsevier.
- Huang, Z., J.F. Keffer, 1996. Development of structure within the turbulent wake of a porous body. Part 1. The initial formation region. *J. Fluid Mech.*, 329, 103-115.
- Julien, P. 1995. *Erosion and Sedimentation*. Cambridge University Press, 280 pp.
- Kravchenko, A.G., P. Moin, 1999. Numerical studies of flow over a circular cylinder at  $Re_D = 3900$ . *Physics of Fluids*, 12 (2), 403-417.
- Leonard, L., M. Luther, 1995. Flow hydrodynamics in tidal marsh canopies. *Limnol. Oceanogr.*, 40(8), 1474-1484.
- Lightbody, A., H. Nepf, 2006. Prediction of velocity profiles and longitudinal dispersion in emergent salt marsh vegetation. *Limnol. Oceanogr.*, 51(1), 218-228.
- Lopez, F., M. Garcia, 1998. Open-channel flow through simulated vegetation: suspended sediment transport modeling. *Water Resour. Res.*, 34 (9), 2341-2352.
- Lyn, D.A., S. Einav, W. Rodi, J.-H. Park, 1995. A laser-Doppler velocimetry study of ensemble-averaged characteristics of the turbulent near wake of a square cylinder. *J. Fluid Mech.*, 304, 285-319.

- Macklin, M., 1996. Fluxes and storage of sediment-associated heavy metals in floodplain systems: assessment and river basin management issues at a time of rapid environmental change. In *Floodplain Processes* (ed. M. Anderson, D. Walling & P. Bates), chap. 13, pp. 441-460. Wiley.
- Massel, S., K. Furukawa, R. Brinkman, 1999. Surface wave propagation in mangrove forests. *Fluid Dyn. Res.* 24:219-249. doi:10.1016/S0169-5983(98)00024-0.
- Mazda, Y., E. Wolanski, B. King, A. Sase, D. Ohtsuka, M. Magi, 1997. Drag force due to vegetation in mangrove swamps. *Mangroves and Salt Marshes*, 1 (3), 193–199.
- Moore, K.A., 2004. Influence of seagrasses on water quality in shallow regions of the lower Chesapeake Bay. *J Coast Res.*, 20 (Special Issue), 162-178.
- Muhar, S., S. Schmutz, M. Jungwirth, 1995. River restoration concepts — goals and perspectives. *Hydrobiologia*, Volume 303, Numbers 1-3, 183-194.
- Nepf, H., 1999. Drag, turbulence and diffusivity in flow through emergent vegetation. *Water Resour. Res.*, 35 (2), 479–489.
- Nepf, H., M. Ghisalberti, B. White, E. Murphy, 2007. Retention time and dispersion associated with submerged aquatic canopies. *Water Res. Res.*, 43, W04422, doi:10.1029/2006WR005362
- Palmer, M., H. Nepf, T. Petterson, J. Ackerman, 2004. Observations of particle capture on a cylindrical collector: Implications for particle accumulation and removal in aquatic systems, *Limnol. Oceanogr.*, 49, 76-85.
- Pope, S. B., 2000. *Turbulent Flows*. Cambridge University Press.
- Rominger, J., H. Nepf, 2011. Flow adjustment and interior flow associated with a rectangular porous obstruction. *J. Fluid Mech.* Under review.
- Roshko, A., 1961. Experiments on the flow past a circular cylinder at very high Reynolds number. *J. Fluid Mech.*, 10, 345-356.
- Sand-Jensen, K., 1998. Influence of submerged macrophytes on sediment composition and near-bed flow in lowlands streams, *Freshwater Biology*, 39(4), 663-679.
- Sand-Jensen, K., M. L. Pedersen, 2008. Streamlining of plant patches in streams. *Freshwater Biology*, 53, 714-726.
- Schewe, G., 1983. On the force fluctuation acting on a circular cylinder in cross-flow from subcritical up to transcritical Reynolds numbers. *J. Fluid Mech.*, 133, 265-285.
- Schlichting, H., 1960. *Boundary Layer Theory*. McGraw-Hill Series in Mechanical Engineering.
- Schultz, M., H.-P. Kozerski, T. Pluntke, K. Rinke, 2003. The influence of macrophytes on sedimentation and nutrient retention in the lower River Spree. *Water Res. Res.*, 37, 569-578.
- Sharpe, R.G., C. S. James, 2006. Deposition of sediment from suspension in emergent vegetation. *Water SA*, 32(2), 211–218.

- Soulsby, R. L., 1997. *Dynamics of marine sands*, Thomas Telford, London
- Stone, B., H. T. Shen, 2002. Hydraulic resistance of flow in channels with cylindrical roughness. *J. Hydr. Eng.* 128(5), ASCE, 500-506.
- Stromberg, J. C., 2001. Restoration of riparian vegetation in the south-western United States: importance of flow regimes and fluvial dynamism. *Journal of Arid Environments*, 49(1), pp 17-34.
- Takemura, T., N. Tanaka, 2007. Flow structures and drag characteristics of a colony-type emergent roughness model mounted on a flat plate in uniform flow. *Fluid Dyn. Res.*, 39, 694, doi:10.1016/j.fluidyn.2007.06.001
- Tanino, Y., H. Nepf, 2008. Lateral dispersion in random cylinder arrays at high Reynolds number. *J. Fluid Mech.*, 600, 339–371.
- Townsend, A. A., 1947. Measurements in the turbulent wake of a cylinder. *Proc. R. Soc. Lond.* 190, 551-561, doi: 10.1098/rspa.1947.0096
- Turker, U., O. Yagci, M. Kabdasli, 2006. Analysis of coastal damage of a beach profile under the protection of emergent vegetation. *Ocean Eng.* 33:810-828.
- Valiela, I., J. Teal, W. Deuser, 1978. The nature of growth forms in the salt marsh grass *Spartina alterniflora*. *Amer. Naturalist*, 112, 461–470.
- White, B. 2006. Momentum and mass transport by coherent structures in a shallow vegetated shear flow. PhD Thesis. Massachusetts Institute of Technology.
- White, B., H. Nepf, 2007. Shear instability and coherent structures in a flow adjacent to a porous layer. *J. Fluid Mech.*, 593, 1–32.
- White, B., H. Nepf, 2008. A vortex-based model of velocity and shear stress in a partially vegetated shallow channel. *Water Resour. Res.*, 44, W01412, doi. 10.1029/2006WR005651.
- Winant, C., F. Browand, 1974. Vortex pairing, the mechanism of turbulent mixing-layer growth, at moderate Reynolds number. *J. Fluid Mech.*, 63, 237-255.
- Windham, L., J. Weis, P. Weis, 2003. Uptake and distribution of metals in two dominant salt marsh macrophytes, *Spartina alterniflora* and *Phragmites australis*, *Estuar. Coast. Shel Sci.*, 56, 63–72.
- Widdows, J., N. Pope, M. Brinsley, 2008. Effect of *Spartina anglica* stems on near-bed hydrodynamics, sediment erodability, and morphological changes on an intertidal mudflat. *Mar. Ecol. Progr. Ser.*, 362, 45-57.
- Wood, C. J., 1967. Visualization of an incompressible wake with base bleed. *J. Fluid Mech.*, 29, part 2, 259-272.
- Zong, L., H. Nepf, 2010. Flow and deposition in and around a finite patch of vegetation. *Geomorphology*, 116 (3), 363-372.